Nonlinear Dyn (2012) 67:859–883
DOI 10.1007/s11071-011-0031-5

ORIGINAL PAPER

Nonlinear damping in a micromechanical oscillator

Stav Zaitsev · Oleg Shtempluck · Eyal Buks ·
Oded Gottlieb

Received: 29 July 2010 / Accepted: 22 March 2011 / Published online: 16 April 2011

Abstract Nonlinear elastic effects play an important role in the dynamics of microelectromechanical systems (MEMS). A Duffing oscillator is widely used as an archetypical model of mechanical resonators with nonlinear elastic behavior. In contrast, nonlinear dissipation effects in micromechanical oscillators are often overlooked. In this work, we consider a doubly clamped micromechanical beam oscillator, which exhibits nonlinearity in both elastic and dissipative properties. The dynamics of the oscillator is measured in both frequency and time domains and compared to theoretical predictions based on a Duffing-like model with nonlinear dissipation. We especially focus on the behavior of the system near bifurcation points. The results show that nonlinear dissipation can have a significant impact on the dynamics of micromechanical systems. To account for the results, we have developed a continuous model of a geometrically nonlinear beam-string with a linear Voigt–Kelvin viscoelastic constitutive law, which shows a relation between linear and nonlinear damping. However, the experimental results suggest that this model alone cannot fully account for all the experimentally observed nonlinear dissipation, and that additional nonlinear dissipative processes exist in our devices.

Keywords MEMS · Duffing oscillator · Nonlinear damping · Saddle-node bifurcation · Parameter identification · Forced vibration

1 Introduction

The field of micro-machining is forcing a profound redefinition of the nature and attributes of electronic devices. This technology allows fabrication of a variety of on-chip fully integrated micromechanical sensors and actuators with a rapidly growing range of applications. In many cases, it is highly desirable to shrink the size of mechanical elements down to the nano-scale [1–4]. This allows enhancing the speed of operation by increasing the frequencies of mechanical resonances and improving their sensitivity as sensors. Furthermore, as devices become smaller, their power consumption decreases and the cost of mass fabrication can be significantly lowered. Some key applications of microelectromechanical systems (MEMS) technology include magnetic resonance force microscopy (MRFM) [5, 6] and mass-sensing [7–10]. Further miniaturization is also motivated by the quest for mesoscopic quantum effects in mechanical systems [11–18].

S. Zaitsev (✉) · O. Shtempluck · E. Buks
Department of Electrical Engineering, Technion–Israel Institute of Technology, Haifa 32000, Israel
e-mail: zzz@tx.technion.ac.il

O. Gottlieb
Department of Mechanical Engineering, Technion–Israel Institute of Technology, Haifa 32000, Israel

Nonlinear effects are of great importance for micromechanical devices. The relatively small applied forces needed for driving a micromechanical oscillator into the nonlinear regime are usually easily accessible [19]. Thus, a variety of useful applications such as frequency synchronization [20], frequency filtering, mixing and conversion [21–23], parametric and intermodulation amplification [24], mechanical noise squeezing [25], stochastic resonance [26], and enhanced sensitivity mass detection [27, 28] can be implemented by applying modest driving forces. Furthermore, monitoring the displacement of a micromechanical resonator oscillating in the linear regime may be difficult when a displacement detector with high sensitivity is not available. Thus, in many cases the nonlinear regime is the only useful regime of operation.

Another key property of systems based on mechanical oscillators is the rate of damping. For example, in many cases the sensitivity of MEMS sensors is limited by thermal fluctuation [7, 29], which is related to damping via the fluctuation dissipation theorem. In general, micromechanical systems suffer from low quality factors Q relative to their macroscopic counterparts [3, 30, 31]. However, very little is currently known about the underlying physical mechanisms contributing to damping in these devices. A variety of different physical mechanisms can contribute to damping, including bulk and surface defects [32, 33], thermoelastic damping [34, 35], nonlinear coupling to other modes, phonon–electron coupling, clamping loss [36, 37], interaction with two level systems [38], etc. Identifying experimentally the contributing mechanisms in a given system can be highly challenging, as the dependence on a variety of parameters has to be examined systematically [39–44].

The archetypical model used to describe nonlinear micro- and nano-mechanical oscillators is the Duffing oscillator [45]. This model has been studied in great depth [45–48], and special emphasis has been given to the dynamics of the system near the bifurcation points [49–54].

In order to describe dissipation processes, a linear damping model is usually employed, either as a phenomenological ansatz, or in the form of linear coupling to thermal bath, which represents the environment. However, nonlinear damping is known to be significant at least in some cases. For example, the effect of nonlinear damping for the case of strictly dissipative force, being proportional to the velocity to the nth power, on the response and bifurcations of driven Duffing [55–58] and other types of nonlinear oscillators [45, 57, 59–61] has been studied extensively. Also, nonlinear damping plays an important role in parametrically excited mechanical resonators [42, 62] where without it, solutions will grow without bound [45, 63].

In spite of the fact that a massive body of literature exists which discusses the nonlinear elastic effects in micro- and nano-mechanical oscillators as well as the consequences of nonlinear damping, the quantitative experimental data on systems with nonlinear damping, especially those nearing bifurcation points, remains scarce. Furthermore, such systems impose special requirements on the experiment parameters and procedures, mainly due to the very slow response times near the bifurcation points. Straightforward evaluation of these requirements by simple measurements can facilitate accurate data acquisition and interpretation.

In the present paper we study damping in a micromechanical oscillator operating in the nonlinear regime excited by an external periodic force at frequencies close to the mechanical fundamental mode. We consider a Duffing oscillator nonlinearly coupled to a thermal bath. This coupling results in a nonlinear damping force proportional to the velocity multiplied by the displacement squared. As will be shown below, this approach is equivalent to the case where the damping nonlinearity is proportional to the velocity cubed [64]. In conjunction with a linear dissipation term, it has also been shown to describe an effective quadratic drag term [65].

We find that nonlinear damping in our micromechanical oscillators is non-negligible, and has a significant impact on the oscillators' response. Furthermore, we develop a theoretical one-dimensional model of the oscillator's behavior near the bifurcation point [46, 49]. Most of the parameters that govern this behavior can be estimated straightforwardly from frequency response measurements alone, not requiring exact measurement of oscillation amplitudes. Measuring these parameters under varying conditions provides important insights into the underlying physical mechanisms [66, 67].

We use our results to estimate different dynamic parameters of an experimentally measured micromechanical beam response, and show how these estimations can be used to increase the accuracy of experimental measurements and to estimate measurement errors. The main source of error is found to be the slowing down behavior near the bifurcation point, also known as the saddle node "ghost" [50]. We also investigate the possibility of thermal escape of the system from a stable node close to the bifurcation point [46, 51, 52, 68, 69] and find that the probability of this event in our experiments is negligible.

Finally, we propose and analyze a continuum mechanics model of our micromechanical oscillator as a planar, weakly nonlinear strongly pre-tensioned, viscoelastic beam-string [70]. The analysis of this model illustrates a possible cause for non-negligible nonlinear damping as observed in the experiment.

2 Experimental setup

For the experiments we employ micromechanical oscillators in the form of doubly clamped beams made of $Pd_{0.15}Au_{0.85}$ as shown in Fig. 1. The device is fabricated on a rectangular silicon-nitride membrane (side length 100–200 μm) by the means of electron beam lithography followed by thermal metal evaporation. The membrane is then removed by electron cyclotron resonance (ECR) plasma etching, leaving the doubly clamped beam freely suspended. The bulk micromachining process used for sample fabrication is similar to the one described in [16]. The dimensions of the beams are: length 100–200 μm, width 0.25–1 μm and thickness 0.2 μm, and the gap separating the beam and the electrode is 5–8 μm.

Measurements of all mechanical properties are done *in situ* by a scanning electron microscope (SEM) (working pressure 10^{-5} Torr), where the imaging system of the microscope is employed for displacement detection [16]. Some of the samples were also measured using an optical displacement detection system described elsewhere [25]. Driving force is applied to the beam by applying a voltage to the nearby electrode. With a relatively modest driving force, the system is driven into the region of nonlinear oscillations [16, 71].

We use a network analyzer for frequency domain measurements, as shown in Fig. 2. For time domain measurements of the slow varying envelope we employ a lock-in amplifier, connected as show in Fig. 3. The mechanical oscillator is excited by a monochromatic wave, whose amplitude is modulated by a square wave with low frequency (20–50 Hz). This results in bursting excitation, which allows measurement of ring-down behavior in time domain. The lock-in amplifier is locked to the excitation frequency, and measures the amplitude of the slow envelope of the oscillator's response. The lock-in amplifier time constant should be much smaller than the ring down time, which is governed by dissipation in the micromechanical system. Typically, in our experiments, the time constant is 100 μs and the characteristic ring down time is 10 ms.

The displacement detection scheme described above is not exactly linear, because the amount of the detected secondary electrons or reflected light is not strictly proportional to the mechanical oscillator am-

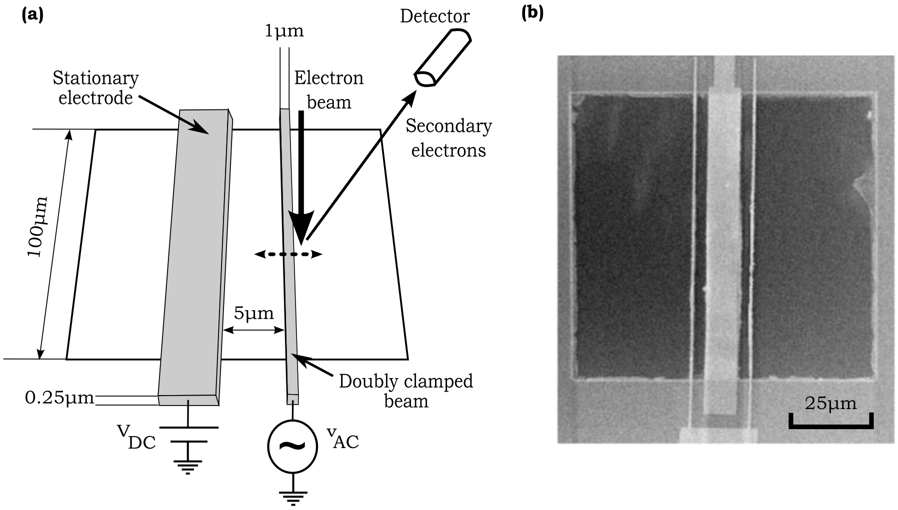

Fig. 1 A typical device consists of a suspended doubly clamped narrow beam (length 200 μm, width 1–0.25 μm, and thickness 0.2 μm) and a wide electrode. The excitation force is applied as voltage between the beam and the electrode. (**a**) Experimental setup and typical sample's dimensions. The direction of the vibration of the micromechanical beam is denoted by dotted arrow. (**b**) SEM micrograph of a device with one wide electrode and two narrow doubly clamped beams

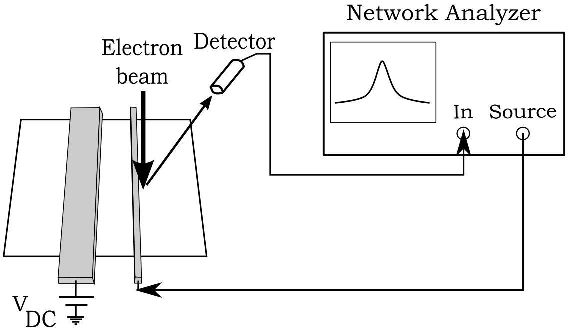

Fig. 2 Network analyzer is used for frequency domain measurements. If the system is excited into a bistable regime, special care should be taken to ensure accurate measurement near bifurcation points, as discussed in Sect. 3.5

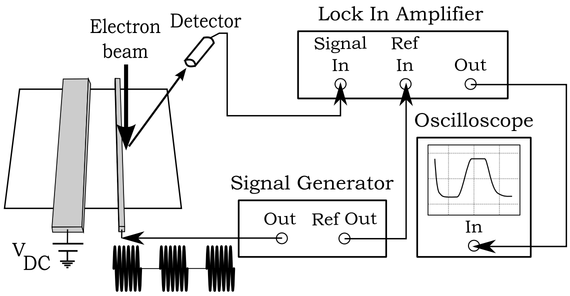

Fig. 3 Lock-in amplifier is employed for time domain measurements. The oscillator is excited at a single frequency. The amplitude of the excitation is modulated by a square wave, effectively turning the excitation on and off 20–50 times per second. Such bursting excitation is used to measure the ringing down of the slow envelope in the time domain

plitude, but merely a monotonic function of the latter. Nonuniform distribution of primary electrons or light power in the spot increases this nonlinearity even further. Thus, some distortion in the measured response amplitude is introduced.

In general, in the experimental setup described above, many different processes can contribute to the mechanical noise of the doubly clamped beam, including, for example, the shot noise of the electron beam in the SEM, and the phase noise of the electrical excitation signal. It can be shown, however, that the impact of these noise sources is negligible compared to the thermal noise of the oscillator itself, which is intimately connected with the mechanical dissipation properties of the oscillator. This connection is treated in the next section.

3 Theory

3.1 Equation of motion

We excite the system close to its fundamental mode. Ignoring all higher modes allows us to describe the dynamics using a single degree of freedom x.

In the main part of this study, no assumptions are made about the source of linear and nonlinear dissipation. The energy dissipation is modeled phenomenologically by coupling the micromechanical oscillator to a thermal bath consisting of harmonic oscillators [72–75]. Physically, several processes may be responsible for mechanical damping [29, 30, 36, 76, 77], including thermoelastic effects [34, 35, 78], friction at grain boundaries [79], bulk and surface impurities [31, 80, 81], electrical losses, clamping loss [37, 82, 83], etc. We also regard the linear and nonlinear damping constants as independent of one another, although they probably result from same physical processes. In Sect. 5.2 we consider one possible model connecting the linear and nonlinear dissipation coefficients, and compare its predictions to experimental data.

The Hamiltonian of the system, which includes the mechanical beam and thermal bath modes coupled to it, is

$$\mathcal{H} = \mathcal{H}_m + \mathcal{H}_b + \mathcal{H}_i, \tag{1}$$

where

$$\mathcal{H}_m = \frac{p^2}{2m} + \tilde{U}(x) + \mathcal{E}_{\mathrm{cap}}(x,t),$$

$$\mathcal{H}_b = \sum_b \left(\frac{p_b^2}{2m_b} + \frac{1}{2} m_b \omega_b^2 q_b^2 \right),$$

$$\mathcal{H}_i = \sum_b \Gamma(x, \omega_b) q_b$$

describe the micromechanical beam, the thermal bath, and the interaction between them, respectively. Here, m is the effective mass of the fundamental mode of the micromechanical beam, and p and x are the effective momentum and displacement of the beam. Also, $\tilde{U}(x)$ is the elastic potential, and $\mathcal{E}_{\mathrm{cap}}(x,t) = C(x)V(t)^2/2$ is the capacitive energy, where $C(x) = C_0/(1 - x/d)$ is the displacement-dependent capacitance, d is the gap between the electrode and the beam, and $V(t)$ is the time-dependent voltage applied between the electrode and the micromechanical beam. The sum $\sum_b$ denotes summing over all relevant thermal bath modes, while ω_b is the frequency of one of the modes in the thermal bath with effective momentum p_b and displacement q_b, and m_b is the effective mass of the same mode. Finally, $\Gamma(x,\omega_b)$ is a function describing the interaction strength of each thermal bath mode with the fundamental mode of the micromechanical beam.

The equations of motion resulting from (1) are

$$m\ddot{x} = -\frac{\partial}{\partial x}\big(\tilde{U}(x) + \mathcal{E}_{\mathrm{cap}}(x,t)\big) - \sum_b q_b \frac{\partial \Gamma(x,\omega_b)}{\partial x}, \tag{2a}$$

$$m_b \ddot{q}_b = -m_b\omega_b^2 q_b - \Gamma(x,\omega_b). \tag{2b}$$

The formal solution of (2b) can be written as

$$\begin{aligned} q_b(t) &= q_{b0}\cos\omega_b t + \frac{\dot{q}_{b0}}{\omega_b}\sin\omega_b t \\ &\quad + \int_0^t \frac{\Gamma(x,\omega_b;\tau)}{m_b\omega_b}\sin\omega_b(\tau - t)\,d\tau, \end{aligned}$$

or, integrating by parts,

$$\begin{aligned} q_b(t) &= q_{b0}\cos\omega_b t + \frac{\dot{q}_{b0}}{\omega_b}\sin\omega_b t \\ &\quad + \frac{\Gamma(x,\omega_b;0)}{m_b\omega_b^2}\cos\omega_b t - \frac{\Gamma(x,\omega_b;t)}{m_b\omega_b^2} \\ &\quad + \int_0^t \frac{\dot{x}(\tau)}{m_b\omega_b^2}\frac{\partial\Gamma(x,\omega_b;\tau)}{\partial x}\cos\omega_b(\tau - t)\,d\tau, \end{aligned} \tag{3}$$

where q_{b0} and $\dot{q}_{b0}$ are the initial conditions of the thermal mode displacement and velocity, respectively; and $\Gamma(x,\omega_b;s)$ denotes the coupling strength function $\Gamma(x,\omega_b)$ evaluated at time s.

Substituting (3) into (2a), one gets

$$\begin{aligned} &m\ddot{x} + \int_0^t \mathcal{K}(x,t,\tau)\dot{x}(\tau)\,d\tau + \frac{\partial U(x)}{\partial x} \\ &\quad = -\frac{\partial \mathcal{E}_{\mathrm{cap}}(x,t)}{\partial x} + mn(t), \end{aligned} \tag{4}$$

where $n(t)$ is the noise,

$$U(x) = \tilde{U}(x) - \sum_b \frac{\Gamma^2(x,\omega_b)}{2m_b\omega_b^2} \tag{5}$$

is the renormalized potential, and

$$\begin{aligned} &\mathcal{K}(x,t,\tau) \\ &\quad = \sum_b \frac{\partial\Gamma(x,\omega_b;t)}{\partial x}\frac{\partial\Gamma(x,\omega_b;\tau)}{\partial x}\frac{\cos\omega_b(\tau - t)}{m_b\omega_b^2} \end{aligned}$$

is the memory kernel [75, 84]. Also, the initial slip term given by

$$\sum_b \Gamma(x,\omega_b;0)\cos\omega_b t\frac{\partial}{\partial x}\Gamma(x,\omega_b;t)/\big(m_b\omega_b^2\big)$$

has been dropped [75]. Finally, the noise autocorrelation for an initial thermal ensemble is

$$\big\langle n(t)n(s)\big\rangle = \frac{k_B T}{m^2}\mathcal{K}(x,t,s),$$

where T is the effective temperature of the bath, and k_B is the Boltzmann constant. The last result is a particular form of the fluctuation-dissipation theorem [85–88].

We employ a nonlinear, quartic potential $U(x) = \frac{1}{2}k_1x^2 + \frac{1}{4}k_3x^4$ in order to describe the elastic properties of the micromechanical beam oscillator. Assuming $\Gamma(x,\omega_b)$ to be polynomial in x, it can be deduced from (5) that only linear and quadratic terms in $\Gamma(x,\omega_b)$ should be taken into account [74, 89], i.e.,

$$\Gamma(x,\omega_b) = g_1(\omega_b)x + \frac{1}{2}g_2(\omega_b)x^2. \tag{6}$$

The memory kernel in this case is

$$\begin{aligned} \mathcal{K}(x,t,\tau) &= \sum_b \Big(g_1^2 + g_1g_2\big(x(t) + x(\tau)\big) \\ &\quad + g_2^2 x(t)x(\tau)\Big)\frac{\cos\omega_b(\tau - t)}{m_b\omega_b^2}. \end{aligned}$$

Making the usual Markovian (short-time noise autocorrelation) approximation [46, 72, 74], i.e., $\mathcal{K}(x,t,s) \propto \delta(t-s)$, one obtains

$$\mathcal{K}(x,t,\tau) = \big(2b_{11} + b_2x + b_{31}x^2\big)\delta(t-\tau),$$

and the equation of motion (4) becomes

$$\begin{aligned} &m\ddot{x} + \big(2b_{11} + b_{31}x^2 + b_{32}\dot{x}^2\big)\dot{x} + k_1x + k_3x^3 \\ &\quad = -\frac{\partial\mathcal{E}_{\mathrm{cap}}(x,t)}{\partial x} + mn(t), \end{aligned} \tag{7}$$

where b_{11} is the linear damping constant, b_{31} and b_{32} are the nonlinear damping constants, k_1 is the linear spring constant and k_3 is the nonlinear spring constant.

Some clarifications regarding (7) are in order. The quadratic dissipation term $b_2 x\dot{x}$ has been dropped from the equation because it has no impact on the first order multiple scales analysis, which will be applied below. An additional dissipation term proportional to the cubed velocity, $b_{32}\dot{x}^3$, has been added artificially. Such term, although not easily derived using the analysis sketched above, may be required to describe some macroscopic friction mechanisms [45, 55, 59], such as losses associated with nonlinear electrical circuits. It will be shown below that the impact of this term on the behavior of the system is very similar to the impact of $b_{31}x^2\dot{x}$.

The applied voltage is composed of large constant (DC) and small monochromatic components, namely, $V(t) = V_{\mathrm{DC}} + v\cos\omega t$. The one-dimensional equation of motion (7) can be rewritten as

$$\ddot{x} + \left(2\gamma_{11} + \gamma_{31}x^2 + \gamma_{32}\dot{x}^2\right)\dot{x} + \omega_0^2 x + \alpha_3 x^3 = \frac{C_0(V_{\mathrm{DC}}^2 + \frac{1}{2}v^2 + 2V_{\mathrm{DC}}v\cos\omega t + \frac{1}{2}v^2\cos 2\omega t)}{2md(1-\frac{x}{d})^2} + n(t), \tag{8}$$

where $\omega_0^2 = k_1/m$, $\gamma_{11} = b_{11}/m$, $\gamma_{31} = b_{31}/m$, $\gamma_{32} = b_{32}/m$, and $\alpha_3 = k_3/m$.

3.2 Slow envelope approximation

In order to investigate the dynamics described by the equation of motion (8) analytically, we use the fact that nonlinearities of the micromechanical oscillator and the general energy dissipation rate are usually small (as shown in Sect. 4, the linear quality factor in our systems has a typical value of several thousands). In the spirit of the standard multiple scales method [45, 48], we introduce a dimensionless small parameter ϵ in (8), and regard the linear damping coefficient $\gamma_{11} \equiv \epsilon\tilde{\gamma}_{11}$, the nonlinear damping coefficients $\gamma_{31} \equiv \epsilon\tilde{\gamma}_{31}$ and $\gamma_{32} \equiv \epsilon\tilde{\gamma}_{32}$, the nonlinear spring constant $\alpha_3 \equiv \epsilon\tilde{\alpha}_3$, and the excitation amplitude $v \equiv \epsilon\tilde{v}$ as small. It is also assumed that the maximal amplitude of mechanical vibrations is small compared to the gap between the electrode and the mechanical beam d, i.e., $x/d \equiv \epsilon x/\tilde{d}$. Also, the frequency of excitation ω is tuned close to the fundamental mode of mechanical vibrations, namely, $\omega = \omega_0 + \sigma$, where $\sigma \equiv \epsilon\tilde{\sigma}$ is a small detuning parameter.

Retaining terms up to first order in ϵ in (8) gives

$$\ddot{x} + \omega_0^2 x + \epsilon\left[\left(2\tilde{\gamma}_{11} + \tilde{\gamma}_{31}x^2 + \tilde{\gamma}_{32}\dot{x}^2\right)\dot{x} + \tilde{\alpha}_3 x^3 - \frac{2}{\tilde{d}}x\left(\ddot{x} + \omega_0^2 x\right)\right] = F + 2\epsilon\tilde{f}_0\cos\omega t, \tag{9}$$

where $F = \frac{C_0 V_{\mathrm{DC}}^2}{2md}$, and $\epsilon\tilde{f}_0 \equiv f_0 = \frac{C_0 V_{\mathrm{DC}} v}{2md}$. We have dropped the noise from the equation of motion, and will reintroduce its averaged counterpart later in the evolution equation (15).

Following [48], we introduce two time scales $T_0 = t$ and $T_1 = \epsilon t$, and assume the following form for the solution:

$$x(t) = x_0(T_0, T_1) + \epsilon x_1(T_0, T_1).$$

It follows to the first order in ϵ that

$$\frac{d}{dt} = \frac{\partial}{\partial T_0} + \epsilon\frac{\partial}{\partial T_1},$$

and (9) can be separated according to different orders of ϵ, giving

$$\frac{\partial^2 x_0}{\partial T_0^2} + \omega_0^2 x_0 = F, \tag{10a}$$

and

$$\frac{\partial^2 x_1}{\partial T_0^2} + \omega_0^2 x_1 = 2\tilde{f}_0\cos(\omega_0 T_0 + \tilde{\sigma}T_1) - \left(2\tilde{\gamma}_{11} + \tilde{\gamma}_{31}x_0^2 + \tilde{\gamma}_{32}\left(\frac{\partial x_0}{\partial T_0}\right)^2\right)\frac{\partial x_0}{\partial T_0} - \tilde{\alpha}_3 x_0^3 + \frac{2F}{\tilde{d}}x_0 - 2\frac{\partial^2 x_0}{\partial T_0 \partial T_1}. \tag{10b}$$

The solution of (10a) is

$$x_0(T_0, T_1) = \frac{F}{\omega_0^2} + \left(a(T_1)e^{j\tilde{\sigma}T_1}e^{j\omega_0 T_0} + \mathrm{c.c.}\right), \tag{11}$$

where a is a complex amplitude and c. c. denotes complex conjugate. The "slow varying" amplitude a varies on a time scale of order T_1 or slower.

The secular equation [45, 48], which follows from substitution of (11) into (10b), is

$$2\omega_0\left(j\dot{a} + (j\gamma_1 - \Delta\omega)a\right) + (3\alpha_3 + j\gamma_3\omega_0)a^2 a^* = f_0,$$

(12)

where

$$\gamma_1 = \gamma_{11} + \gamma_{31}\frac{F^2}{2\omega_0^4}, \tag{13a}$$

$$\gamma_3 = \gamma_{31} + 3\omega_0^2\gamma_{32}, \tag{13b}$$

and

$$\Delta\omega = \sigma - \Delta\omega_0,$$

where

$$\Delta\omega_0 = \frac{F}{\omega_0}\left(\alpha_3\frac{3F}{2\omega_0^4} - \frac{1}{d}\right) \tag{14}$$

represents a constant shift in linear resonance frequency due to the constant electrostatic force F. Equation (12) is also known as evolution equation. Note that we have returned to the full physical quantities, i.e., dropped the tildes, for convenience. Also, one must always bear in mind that the accuracy of the evolution equation is limited to the assumptions considered at the beginning of this section.

As was mentioned earlier, both nonlinear dissipation terms give rise to identical terms in the evolution equation (12). Therefore, the behavior of these two dissipation cases is similar near the fundamental resonance frequency ω_0. Also, note that linear dissipation coefficient γ_1 (13a) is not constant, but is rather quadratically dependent on the constant electrostatic force F due to the nonlinear dissipation term γ_{31}.

The secular equation (12) can be written as

$$j\dot{a} + (j\gamma_1 - \Delta\omega)a + q(1 + jp)a^2a^* = \frac{1}{2\omega_0}\big(f_0 + n_{\text{slow}}(t)\big), \tag{15}$$

where dot denotes differentiation with respect to (slow) time,

$$q = \frac{3\alpha_3}{2\omega_0}, \tag{16}$$

$$p = \frac{\gamma_3\omega_0}{3\alpha_3}, \tag{17}$$

and $n_{\text{slow}}(t)$ is the averaged noise process with the following characteristics [46, 53]:

$$\langle n_{\text{slow}}(t)\rangle = 0, \tag{18a}$$

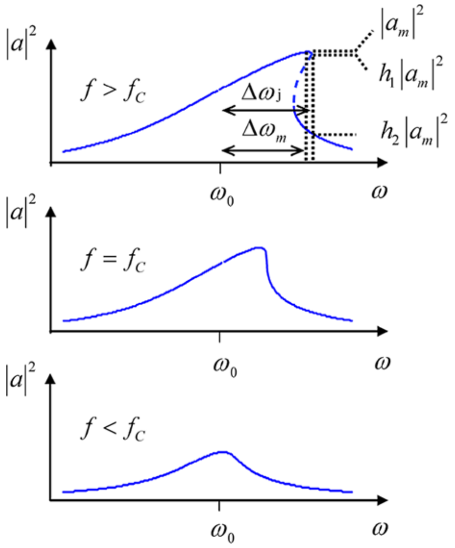

Fig. 4 Steady-state solutions under different excitation amplitudes f_0. In case $f_0 < f_C$ (where f_C is some critical excitation force, dependent on the system parameters, see text), only one real solution exists and no bistability is possible. In case $f_0 = f_C$, the system is on the edge of bistability and one point exists, where $|a|^2$ vs. ω has an infinite slope. In case $f_0 > f_C$, the system is in bistable regime having three real solutions over some range of frequencies. Two of these solutions are stable. *The dashed line* denotes the unstable solution

$$\langle n_{\text{slow}}(t)n_{\text{slow}}(s)\rangle = N\delta(t - s), \tag{18b}$$

$$N = \frac{k_BT}{m}\big(\gamma_1 + \gamma_3|a|^2\big). \tag{18c}$$

The steady-state amplitude can be found by setting $\dot{a} = 0$, $n_{\text{slow}} = 0$ and taking a square of the evolution equation (15), resulting in

$$q^2(1 + p^2)|a|^6 + 2q(\gamma_1 p - \Delta\omega)|a|^4 + \big(\gamma_1^2 + \Delta\omega^2\big)|a|^2 - \frac{f_0^2}{4\omega_0^2} = 0. \tag{19}$$

This cubic equation of $|a|^2$ can have either one, two, or three different real roots, depending on the values of the detuning parameter $\Delta\omega$ and the excitation amplitude f_0. When γ_3 is sufficiently small, i.e., $p \to 0$, the solutions of (19) behave very much like the ordinary Duffing equation solutions, to which (7) reduces if $b_{31} = 0$ and $b_{32} = 0$ (see Fig. 4).

The solution of (15) can be also presented in polar form [45]:

$$a = Ae^{j\phi}, \tag{20}$$

where A and ϕ are real, and A is assumed to be positive. Separating the real and imaginary parts of (15), one obtains (omitting the noise)

$$\dot{A} + \gamma_1 A + qpA^3 = -\frac{f_0}{2\omega_0}\sin\phi, \tag{21a}$$

$$A\dot{\phi} + \Delta\omega A - qA^3 = -\frac{f_0}{2\omega_0}\cos\phi. \tag{21b}$$

Steady-state solutions are defined by $\dot{A} = 0$, $\dot{\phi} = 0$, which results in (19).

The maximal amplitude $|a_m|^2$ can be found from (19) by requiring

$$\left.\frac{d(|a|^2)}{d\Delta\omega}\right|_{\Delta\omega=\Delta\omega_m} = 0,$$

where $\Delta\omega_m$ is the corresponding excitation frequency detuning. This results in

$$\frac{\Delta\omega_m}{|a_m|^2} = q = \frac{3\alpha_3}{2\omega_0}. \tag{22}$$

Interestingly enough, the phase ϕ of the maximal response is always equal $-\pi/2$, i.e., the maximal response is exactly out of phase with the excitation regardless the magnitude of the excitation, a feature well known for the linear case. This general feature can be explained as follows. For an arbitrary response amplitude A, there exist either two or no steady-state ϕ solutions of (21). If two solutions ϕ_1 and ϕ_2 exist, they must obey $\phi_2 = \pi - \phi_1$, as seen from (21a). It follows from (21b) that these two solutions correspond to two different values of $\Delta\omega$. However, at the point of maximum response the two solutions coincide, resulting in $\phi_1 = \phi_2 = -\pi/2$, i.e.,

$$a_m = -j|a_m|. \tag{23}$$

The system's behavior qualitatively changes when parameters such as the excitation amplitude and the frequency detuning are varied, as seen in Fig. 4. The parameter values at which these qualitative changes occur are called bifurcation (jump) points [50].

A jump in amplitude is characterized by the following condition:

$$\frac{d(|a|^2)}{d\Delta\omega} \to \pm\infty,$$

or, alternatively,

$$\frac{d\Delta\omega}{d(|a|^2)} = 0.$$

Applying this condition to (19) yields

$$3q^2(1+p^2)|a_j|^4 + 4q(\gamma_1 p - \Delta\omega_j)|a_j|^2 + (\gamma_1^2 + \Delta\omega_j^2) = 0, \tag{24}$$

where $\Delta\omega_j$ and a_j denote the frequency detuning and the amplitude at the jump point, respectively.

When the system is on the edge of bistability, the two jump points coincide and (24) has a single real solution at the point of critical frequency $\Delta\omega_c$ and critical amplitude a_c. The driving force at the critical point is denoted in Fig. 4 as f_C. This point is defined by two conditions:

$$\frac{d\Delta\omega}{d(|a|^2)} = 0,$$

$$\frac{d^2\Delta\omega}{d(|a|^2)^2} = 0.$$

By applying these conditions one finds

$$\Delta\omega_c = \frac{3q}{2}(1+p^2)|a_c|^2 + \gamma_1 p,$$

where a_c is the corresponding critical amplitude. Substituting the last result back into (24), one finds [53]:

$$|a_c|^2 = \frac{2\gamma_1}{\sqrt{3}q}\frac{\sqrt{3}p \pm 1}{1-3p^2}, \tag{26a}$$

$$\Delta\omega_c = \gamma_1 \frac{4p \pm \sqrt{3}(1+p^2)}{1-3p^2}, \tag{26b}$$

$$p = \frac{\Delta\omega_c \mp \sqrt{3}\gamma_1}{\gamma_1 \pm \sqrt{3}\Delta\omega_c}, \tag{26c}$$

where the upper sign should be used if $\alpha_3 > 0$, and the lower sign otherwise. In general, γ_3 is always positive, but α_3 can be either positive or negative. Therefore, q and p are negative if $\alpha_3 < 0$ (soft spring), and positive if $\alpha_3 > 0$ (hard spring).

It follows from (26a) that the condition for the critical point to exist is

$$|p| < \frac{1}{\sqrt{3}}.$$

Without loss of generality, we will focus on the case of "hard" spring, i.e., $\alpha_3 > 0$, $q > 0$, $p > 0$, as this is the case encountered in our experiments.

3.3 Behavior near bifurcation points

When the system approaches the bifurcation points, it exhibits some interesting features not existent elsewhere in the parametric phase space. In order to investigate the system's behavior in the vicinity of the jump points, it is useful to rewrite the slow envelope evolution equation (15) as a two-dimensional flow

$$\dot{x} = f(x, y) + n_x(t), \tag{27a}$$

$$\dot{y} = g(x, y) + n_y(t), \tag{27b}$$

where we have defined $x(t) = \mathrm{Re}\{a\},\ \ y(t) = \mathrm{Im}\{a\}$ (i.e., $a(t) = x(t) + jy(t)$), and

$$f(x, y) = -\gamma_1 x + \Delta\omega y - q\left(x^2 + y^2\right)(y + px), \tag{28a}$$

$$g(x, y) = -\Delta\omega x - \gamma_1 y + q\left(x^2 + y^2\right)(x - py) - \frac{f_0}{2\omega_0}. \tag{28b}$$

The real-valued noise processes $n_x(t)$ and $n_y(t)$ have the following statistical properties:

$$\langle n_x(t)\rangle = \langle n_y(t)\rangle = 0, \tag{29a}$$

$$\langle n_x(t)n_y(t)\rangle = 0, \tag{29b}$$

$$\langle n_x(t)n_x(s)\rangle = \langle n_y(t)n_y(s)\rangle = \frac{N}{8\omega_0^2}\delta(t-s). \tag{29c}$$

At the fixed points, the following holds: $f(x, y) = g(x, y) = 0$. A typical phase space flow of the oscillator in bistable regime is shown in Fig. 5.

For small displacements near an arbitrary fixed point $a_0 = (x_0, y_0)$, namely, $x = x_0 + \Delta x$ and $y = y_0 + \Delta y$, where $\Delta x \ll x_0$ and $\Delta y \ll y_0$, the above nonlinear flow map can be approximated by its linearized counterpart

$$\begin{pmatrix}\Delta\dot{x}\\ \Delta\dot{y}\end{pmatrix} = M\begin{pmatrix}\Delta x\\ \Delta y\end{pmatrix} + \begin{pmatrix}n_x\\ n_y\end{pmatrix}, \tag{30}$$

where

$$M = \begin{pmatrix}f_x & f_y\\ g_x & g_y\end{pmatrix}, \tag{31}$$

and the excitation frequency detuning $\Delta\omega$, as well as the external excitation amplitude f_0, is considered constant. The subscripts in the matrix elements denote partial derivatives evaluated at (x_0, y_0), for example,

$$f_x \equiv \left.\frac{\partial f}{\partial x}\right|_{\substack{x=x_0,\\ y=y_0}}.$$

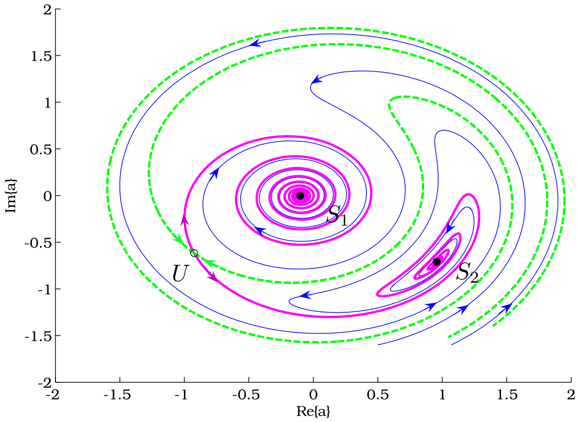

Fig. 5 (Color online) Slow envelope phase plane trajectories of a nonlinear oscillator in bistable regime. Three real solutions of (19) correspond to three fixed points of the flow. S_1 and S_2 are stable spiral nodes, whereas U is the saddle-node, from which two manifolds emerge [50]. The *green dotted line* is the stable manifold ("separatrix"), which separates different basins of attraction, belonging to different stable nodes S_1 and S_2. The *magenta thick line* is the unstable manifold. Two typical phase plane trajectories are shown by arrowed *thin blue lines*

The matrix M is, therefore, the Jacobian matrix of the system (27) evaluated at the point (x_0, y_0). It is straightforward to show that

$$f_x = -\gamma_1 - qp\left(x_0^2 + y_0^2\right) - 2qx_0(y_0 + px_0), \tag{32a}$$

$$f_y = \Delta\omega - q\left(x_0^2 + y_0^2\right) - 2qy_0(y_0 + px_0), \tag{32b}$$

$$g_x = -\Delta\omega + q\left(x_0^2 + y_0^2\right) + 2qx_0(x_0 - py_0), \tag{32c}$$

$$g_y = -\gamma_1 - qp\left(x_0^2 + y_0^2\right) + 2qy_0(x_0 - py_0). \tag{32d}$$

Two important relations follow immediately:

$$f = g_y x - g_x y, \tag{33a}$$

$$g = f_x y - f_y x - \frac{f_0}{2\omega_0}. \tag{33b}$$

The linearized system (30) retains the general qualitative structure of the flow near the fixed points [50], in particular both eigenvalues of the matrix M are negative at the stable nodes, denoted as S_1 and S_2 in Fig. 5.

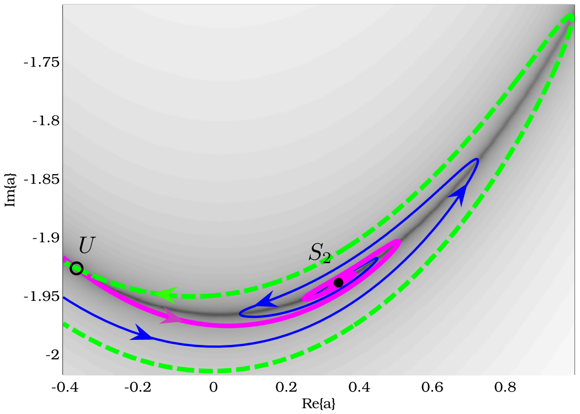

Fig. 6 (Color online) The phase plane geometry when the saddle-node (U) and the stable node (S_2) are well separated. *The green dotted line* is the stable manifold ("separatrix") and the *magenta thick line* is the unstable manifold. A typical phase plane trajectory is shown by the arrowed *thin blue line*. The absolute value of slow envelope's rate of change $\dot{a}$ is represented by the background color. The darkest parts correspond to the slowest motion in the phase space. At both fixed points U and S_2 the value of $\dot{a}$ is zero

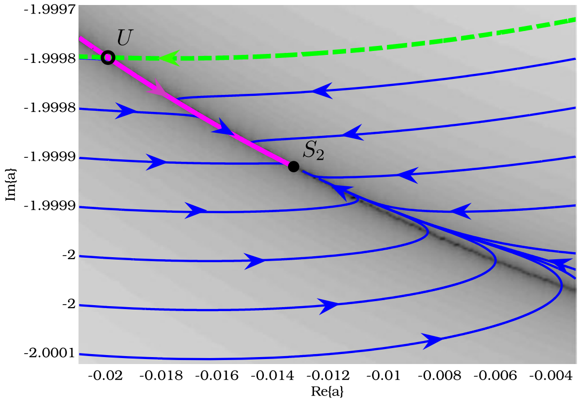

Fig. 7 The phase plane geometry when the saddle-node (U) and the stable node (S_2) are close one to another. *The green dotted line* is the stable manifold ("separatrix"), and *the magenta thick line* is the unstable manifold. Phase plane trajectories are shown by the *thin blue lines*. The absolute value of $\dot{a}$ is represented by the background color. *The darkest* parts correspond to the slowest motion in the phase space. At both fixed points U and S_2, the value of $\dot{a}$ is zero. Note that the motion in the phase space becomes essentially one-dimensional and slows down significantly in the vicinity of the stable node S_2

At the saddle node U, which is not stable, one eigenvalue of M is positive, whereas the other is negative.

The discussed Duffing like systems exhibit saddle point bifurcations. At the bifurcation, one of the stable nodes and the saddle node coincide, resulting in a zero eigenvalue in M. The bifurcation ("jump") point condition is, therefore, $\det M = 0$, which gives the same result as in (24). The case of well-separated stable node and saddle node is shown in Fig. 6, and the case of almost coinciding stable and not stable fixed points is shown in Fig. 7, where the oscillator is on the verge of bifurcation.

We note that in general

$$\operatorname{Tr} M = f_x + g_y = -2\left(\gamma_1 + 2qp|a_0|^2\right),$$

and the slow eigenvalue near the bifurcation point can be estimated as

$$\begin{aligned}\lambda_{\mathrm{sd}} &\approx \left(\cancelto{0}{\frac{\det M}{\operatorname{Tr} M}} + \frac{\partial}{\partial \Delta\omega}\frac{\det M}{\operatorname{Tr} M}\cdot\delta\right)_{\substack{\Delta\omega=\Delta\omega_j,\\ a=a_j}}\\ &= \frac{2q|a_j|^2 - \Delta\omega_j}{\gamma_1 + 2qp|a_j|^2}\delta,\end{aligned}$$

where δ is a small frequency detuning from $\Delta\omega_j$, i.e., $\Delta\omega = \Delta\omega_j + \delta$, $|\delta| \ll |\Delta\omega_j|$. If the system in a bistable regime is close to a bifurcation then $\lambda_{\mathrm{sd}} \to 0$ and the evolution of the system almost comes to a stagnation, phenomenon often referred to as critical slowing down [53]. The motion in the vicinity of the stable node becomes slow and essentially one-dimensional along the unstable manifold. We now turn to show this analytically.

At the bifurcation points the matrix M is singular, i.e., $\det M = 0$. Consequently, the rows of the matrix are linearly dependent, i.e.,

$$M = \begin{pmatrix} f_x & f_y \\ r f_x & r f_y \end{pmatrix},$$

where r is some real constant. Using the last result, we may rewrite (33a) at the bifurcation point as

$$r(f_y x - f_x y) = 0,$$

where we have used the fact that at any fixed point (stable or saddle-node) $f(x, y) = g(x, y) = 0$. However, according to (33b), at any fixed point $f_y x - f_x y = -f_0/2\omega_0 \neq 0$. Therefore, $r = 0$ at the bifurcation point, and the matrix M can be written as

$$M = \lambda_f \begin{pmatrix} 1 & K \\ 0 & 0 \end{pmatrix}, \tag{34}$$

where

$$\lambda_f = -2\left(\gamma_1 + 2qp|a_j|^2\right), \tag{35a}$$

$$K=\frac{f_y}{f_x}=\frac{\gamma_1+2qp|a_j|^2}{2q|a_j|^2-\Delta\omega_j}. \tag{35b}$$

It also follows from (33a) that

$$\frac{y_j}{x_j}=\lim_{\Delta\omega\to\Delta\omega_j}\frac{g_y}{g_x}=\frac{\gamma_1+qp|a_j|^2}{\Delta\omega_j-q|a_j|^2}. \tag{36}$$

Due to the singularity of matrix M at the bifurcation point, a second-order Taylor expansion must be used. The flow map (27) can be approximated near the bifurcation point by

$$\begin{aligned}\Delta\dot{x}&=\lambda_f(\Delta x+K\Delta y)+f_\delta\delta\\&\quad+\frac{1}{2}\left(\delta\frac{\partial}{\partial\Delta\omega}+\Delta x\frac{\partial}{\partial x}+\Delta y\frac{\partial}{\partial y}\right)^2 f\\&\quad+n_x(t),\end{aligned} \tag{37a}$$

$$\begin{aligned}\Delta\dot{y}&=g_\delta\delta+\frac{1}{2}\left(\delta\frac{\partial}{\partial\Delta\omega}+\Delta x\frac{\partial}{\partial x}+\Delta y\frac{\partial}{\partial y}\right)^2 g\\&\quad+n_y(t),\end{aligned} \tag{37b}$$

where all the derivatives denoted by subscripts are evaluated at the jump point $a=a_j$, and

$$f_\delta=y_j,$$

$$g_\delta=-x_j.$$

The above system of differential equations (37) can be simplified by using the following rotation transformation, shown in Fig. 8:

$$\begin{pmatrix}\xi\\\eta\end{pmatrix}=\begin{pmatrix}\cos\alpha & \sin\alpha\\-\sin\alpha & \cos\alpha\end{pmatrix}\begin{pmatrix}\Delta x\\\Delta y\end{pmatrix}, \tag{38}$$

where $\tan\alpha=K$. In these new coordinates, the system (37) becomes

$$\dot{\xi}=\lambda_f\xi+\Omega_\xi\delta+\frac{1}{2}\mathrm{D}^2H(\xi,\eta)+n_\xi(t), \tag{39a}$$

$$\dot{\eta}=-\lambda_fK\xi+\Omega_\eta\delta+\frac{1}{2}\mathrm{D}^2E(\xi,\eta)+n_\eta(t), \tag{39b}$$

where

$$H(\xi,\eta)=f(\xi,\eta)\cos\alpha+g(\xi,\eta)\sin\alpha,$$

$$E(\xi,\eta)=g(\xi,\eta)\cos\alpha-f(\xi,\eta)\sin\alpha,$$

$$\Omega_\xi=y_j\cos\alpha-x_j\sin\alpha,$$

$$\Omega_\eta=-x_j\cos\alpha-y_j\sin\alpha,$$

and D is the differentiation operator

$$\begin{aligned}\mathrm{D}&=\left(\xi\frac{\partial}{\partial\xi}+\eta\frac{\partial}{\partial\eta}+\delta\frac{\partial}{\partial\Delta\omega}\right)\\&=\left(\Delta x\frac{\partial}{\partial x}+\Delta y\frac{\partial}{\partial y}+\delta\frac{\partial}{\partial\Delta\omega}\right).\end{aligned}$$

The noise processes $n_\xi(t)$ and $n_\eta(t)$ have the same statistical properties (29) as $n_x(t)$ and $n_y(t)$.

The time evolution of the system described by the differential equations (39) has two distinct time scales. Motion along the coordinate ξ is "fast", and settling time is of order $|\lambda_f|^{-1}$. The time development along the coordinate η, however, is much slower, as will be shown below.

On a time scale much longer than $|\lambda_f|^{-1}$, the coordinate ξ can be regarded as not explicitly dependent on time. The momentary value of ξ can be approximated as

$$\xi=-\frac{1}{\lambda_f}\left(\Omega_\xi\delta+\frac{1}{2}\frac{\partial^2H}{\partial\eta^2}\eta^2\right), \tag{40}$$

where we have neglected all terms proportional to δ^2 and $\delta\eta$.

The motion along the coordinate η is governed by a slow evolution equation (39b), combining which with

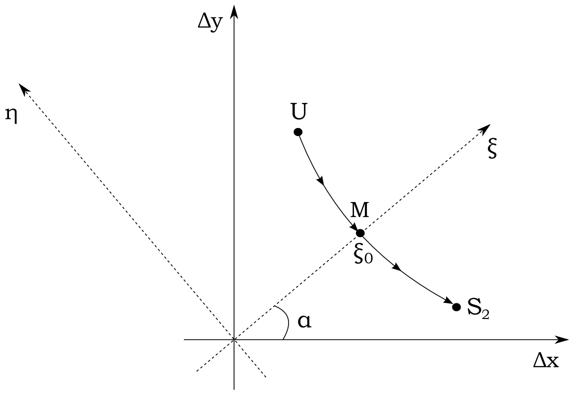

Fig. 8 The effective one-dimensional flow in the vicinity of a bifurcation point. The origin of the phase plane coincides with the bifurcation point. U is the saddle point, and S_2 is a stable node. The effective flow between these two points, marked by arrows, is almost parallel to the rotated coordinate η, while the rotated coordinate ξ remains essentially constant, $\xi=\xi_0+O(\eta^2)$. α is the angle of coordinate rotation. The velocity of the flow is largest at the point M, between the saddle point and the stable node

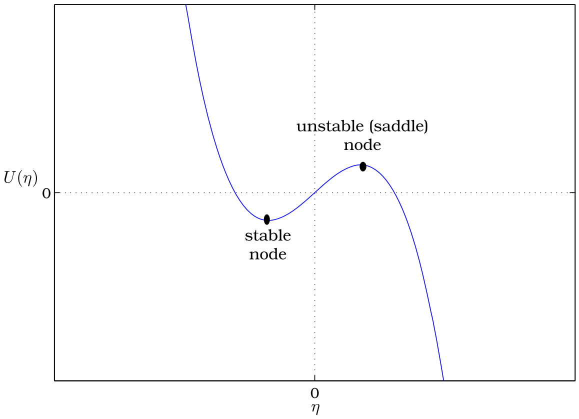

Fig. 9 Effective one-dimensional potential $U(\eta) \propto -\eta(\dot{\eta}_0 + \frac{1}{3}B\eta^2)$, (43)

(40) results in

$$\dot{\eta} = \dot{\eta}_0 + B\eta^2 + n_\eta(t), \tag{41}$$

where

$$\dot{\eta}_0 = -\frac{x_j}{\cos\alpha}\delta, \tag{42a}$$

$$B = \frac{q}{\cos\alpha}\big[x_j\big(1 + 2\sin^2\alpha + p\sin 2\alpha\big) - y_j\big(p\big(1 + 2\cos^2\alpha\big) + \sin 2\alpha\big)\big]. \tag{42b}$$

Note that the noise process $n_\xi(t)$ does not play a significant role in the dynamics of the system, because the system is strongly confined in ξ direction. Such noise squeezing is a general feature of systems nearing saddle-point bifurcation [26, 53, 90, 91].

Two qualitatively different cases of (41) should be recognized. The first case is of a system in a bistable regime with a stable (quasi-stable, as we will see below) and non-stable (saddle) fixed points close enough to a bifurcation point. In this case, the one-dimensional motion is equivalent to a motion of a massless particle in a confining cubic "potential"

$$U(\eta) = -\eta\left(\dot{\eta}_0 + \frac{1}{3}B\eta^2\right), \tag{43}$$

as shown in Fig. 9. Figure 10 depicts the location of the fixed points and the bifurcation point on a frequency response curve in this case. Figure 11 shows a comparison between the exact simulation of the system's motion near the bifurcation point and the analytical result (41).

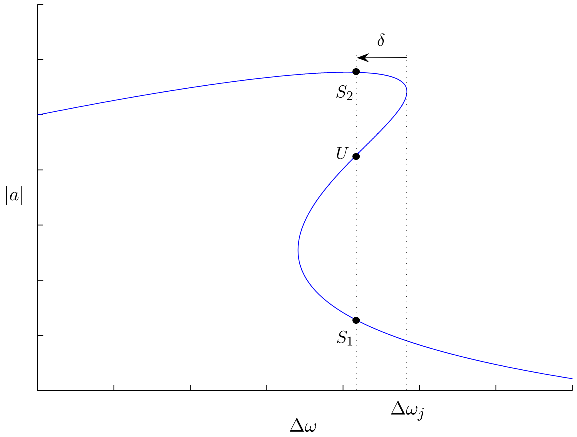

Fig. 10 The location of stable nodes S_1 and S_2, and a saddle node U in a bistable regime close to a bifurcation point. δ, which is negative in this case, is the frequency difference between the excitation frequency and the jump point frequency $(\omega_0 + \Delta\omega_0) + \Delta\omega_j$. The scales of the axes are arbitrary

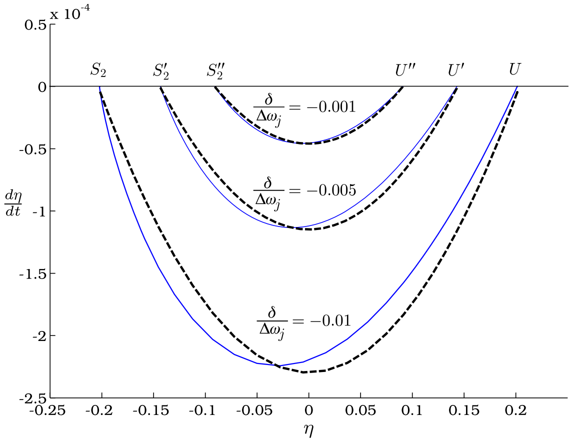

Fig. 11 Velocity along the slow coordinate η for different values of detuning δ. $\Delta\omega_j$ is the jump point (bifurcation) detuning. $p = 0.3/\sqrt{3}$ in all cases, U, U' and U'' are the saddle node positions for different values of δ. Similarly, S_2, S_2' and S_2'' are the stable node positions for different values of δ. Exact values of $d\eta/dt$ are shown by *solid lines. The dashed lines* are the results of analytical approximation (41). The scales of the axes are arbitrary

The quasi one-dimensional system described above is obviously not stable [51, 68, 92]. The rate of escape from the vicinity of the quasi-stable fixed point is [92, 93]

$$r_{\text{therm}}(\delta) \approx \frac{\omega_A\omega_B}{2\pi}e^{-\frac{\Delta U}{D}},$$

where

$$\Delta U = \frac{4}{3}\sqrt{-\frac{\dot{\eta}_0^3}{B}},$$

$$D = \frac{N}{16\omega_0^2} = \frac{k_B T}{16 m\omega_0^2}\left(\gamma_1 + \gamma_3 |a_j|^2\right),$$

$$\omega_A^2 = \left.\frac{\partial^2 U}{\partial \eta^2}\right|_{\text{stable node}} = 2\sqrt{-\dot{\eta}_0 B},$$

$$\omega_B = -\omega_A.$$

Characteristic time of thermal escape τ_{therm} can be shown to be [46]:

$$\tau_{\text{therm}}(\delta) = \frac{1}{r_{\text{therm}}} \approx \tau_0 e^{\frac{\Delta}{k_B T}}, \tag{44a}$$

where

$$\tau_0 = \frac{\pi}{\sqrt{-\dot{\eta}_0 B}} \propto (-\delta)^{-\frac{1}{2}}, \tag{44b}$$

$$\Delta = \frac{64}{3}\frac{m\omega_0^2}{\gamma_1 + \gamma_3 |a_j|^2}\sqrt{\frac{-\dot{\eta}_0^3}{B}} \propto (-\delta)^{\frac{3}{2}}. \tag{44c}$$

This is a mean time in which the system escapes from the stable node near bifurcation point to the other stable solution of (15) due to thermal noise $n_\eta(t)$, and the $3/2$ power law is correct as long as $\Delta \gg k_B T$ [52].

The second case describes a system which has undergone saddle bifurcation, i.e., an annihilation of the stable and non-stable points has occurred. The phase plane motion close to the bifurcation point is still one-dimensional; however, $\dot{\eta}_0$ changes its sign. Therefore, the motion is not confined anymore, but is still very slow in the vicinity of the bifurcation point, because $\dot{\eta}_0 \propto \delta$, as follows from (42a). The system starts converging to the single remaining stable fixed point, but is significantly slowed down, and lingers in the vicinity of the bifurcation point due to the saddle node "ghost". As the system spends most of its time of convergence near the saddle node "ghost", this slow time of convergence τ_{sd} can be roughly estimated as [50]:

$$\tau_{\text{sd}} = \int_0^\infty \frac{d\eta}{\dot{\eta}_0 + B\eta^2} = \frac{\pi}{2\sqrt{\dot{\eta}_0 B}}. \tag{45}$$

Note that $\tau_{\text{sd}} \propto \delta^{-\frac{1}{2}}$, due to (42a).

3.4 Extraction of parameters from experimental data

The analytical results presented above allow us to use data acquired in relatively simple experiments in order to estimate several important dynamic parameters of the micromechanical beam. We note that data acquisition using e-beam or optical beam interaction with vibrating elastic element does not readily enable extraction of displacement values. In contrast, the frequencies of important dynamical features, including maximum and jump points, can be measured with high accuracy using standard laboratory equipment, such as network analyzers and lock-in amplifiers. Therefore, it is desirable to be able to extract as much data as possible from the frequency measurements.

If the system can be brought to the verge of bistable regime, i.e., $f_0 = f_c$, the nonlinear damping parameter p can be readily determined using (26c). The same coefficient can also be extracted from the measurements of the oscillator's frequency response in the bistable regime. In general, the sum of the three solutions for $|a|^2$ at any given frequency can be found from (19). This is employed for the jump point at $\omega_0 + \Delta\omega_0 + \Delta\omega_j$ seen in Fig. 4. Using (22) to calibrate the measured response at this jump point, one has

$$(2h_1 + h_2)|a_m|^2 = -\frac{2q(\gamma_1 p - \Delta\omega_j)}{q^2(1 + p^2)},$$

or

$$(2h_1 + h_2)\,\Delta\omega_m\left(1 + p^2\right) + 2(\gamma_1 p - \Delta\omega_j) = 0, \tag{46}$$

where h_1 and h_2 are defined in Fig. 4. Due to the frequency proximity between the maximum point and the jump point at $\omega = \omega_0 + \Delta\omega_0 + \Delta\omega_j$, the inaccuracy of such a calibration is small. Moreover, as long as excitation amplitude is high enough, h_2 is much smaller than h_1 and even considerable inaccuracy in h_2 estimation will not have any significant impact. This equation can be used to estimate p for different excitation amplitudes at which the micromechanical oscillator exhibits bistable behavior, i.e., $f_0 > f_c$. It is especially useful if the system is strongly nonlinear and cannot be measured near its critical point due to high noise floor or low sensitivity of the displacement detectors used.

Another method for estimating the value of p requires measurement of free ring down transient of the micromechanical oscillator and can be employed also at low excitations, when the system does not exhibit bistable behavior, i.e., $f_0 < f_c$. The polar form of the evolution equation (21) is especially well suited for the analysis of the system's behavior in time domain. Starting from (21a) and applying the free ring down condition $f_0 = 0$, one finds

$$A^2(t) = \frac{A_0^2 e^{-2\gamma_1 t}}{1 + \frac{qp}{\gamma_1} A_0^2 (1 - e^{-2\gamma_1 t})}, \tag{47}$$

where A_0 is the amplitude at $t = 0$. In particular, consider a case in which the system is excited at its maximal response frequency detuning $\Delta\omega_m$, i.e., $A_0^2 = |a_m|^2$. Then, after turning the excitation off, the amplitude during the free ring down process described by (47) can be written as

$$\frac{A^2(t)}{|a_m|^2} = \frac{e^{-2\gamma_1 t}}{1 + p\frac{\Delta\omega_m}{\gamma_1}(1 - e^{-2\gamma_1 t})}. \tag{48}$$

The ring down amplitude measured in time domain can be fitted to the last result.

In addition to nonlinear damping parameter p, most parameters defined above can be easily estimated from frequency measurements near the jump point shown in Fig. 4 if the following conditions are satisfied. The first condition is

$$\left|\frac{\Delta\omega_j - \Delta\omega_m}{\Delta\omega_j}\right| \ll 1, \tag{49a}$$

which can be satisfied by exciting the micromechanical beam oscillator in the bistable regime strongly enough, i.e., $f_0 \gg f_c$. The immediate consequence of the first condition is

$$\frac{|a_m|^2 - |a_j|^2}{|a_j|^2} \ll 1, \tag{49b}$$

i.e., $h_1 \approx 1$, as described above.

Using (49b), it follows from (22) that $q|a_j|^2 \approx \Delta\omega_m$. From the last result and from (35), (36), and (38), the following approximations follow immediately:

$$K \equiv \tan\alpha \approx \frac{\gamma_1}{\Delta\omega_m} + 2p, \tag{50a}$$

$$\lambda_{\mathrm{sd}} = \frac{1}{K}\delta, \tag{50b}$$

$$\lambda_f \approx -2(\gamma_1 + 2p\Delta\omega_m), \tag{50c}$$

$$\frac{y_j}{x_j} \approx \frac{\gamma_1 + p\Delta\omega_m}{\Delta\omega_j - \Delta\omega_m}. \tag{50d}$$

As shown in Sect. 3.2, (23), at the maximum response point $\Delta\omega = \Delta\omega_m$, the following holds: $a_m = -j|a_m|$. Therefore, in view of our assumptions described above, we may write

$$x_j \approx -|a_j|\left(\frac{y_j}{x_j}\right)^{-1}.$$

Consequently,

$$\dot{\eta}_0 \approx |a_j|\left(\frac{y_j}{x_j}\right)^{-1}\sqrt{1 + K^2}\,\delta, \tag{51a}$$

and

$$B \approx \frac{\Delta\omega_m}{|a_j|(1 + K^2)^{\frac{3}{2}}}\left(\frac{y_j}{x_j}\right)^{-1}\left[2K\left(\frac{y_j}{x_j}\right) - 3K^2 - 1 + p\left(\left(3 + K^2\right)\left(\frac{y_j}{x_j}\right) - 2K\right)\right], \tag{51b}$$

which follows from (42). The time τ_{sd}, which describes the slowing down near the saddle-node "ghost" described above (45), can be expressed as

$$\tau_{\mathrm{sd}}(\delta) = \frac{\pi Y}{2\sqrt{\delta}}, \tag{52}$$

where

$$Y \equiv \sqrt{\frac{\delta}{B\dot{\eta}_0}} \approx \frac{1 + K^2}{\sqrt{\Delta\omega_m}} \times \frac{\left(\frac{y_j}{x_j}\right)}{\sqrt{2K\left(\frac{y_j}{x_j}\right) - 3K^2 - 1 + p\left((3 + K^2)\left(\frac{y_j}{x_j}\right) - 2K\right)}}. \tag{53}$$

Finally, we turn to estimate the value of the thermal escape time τ_{therm} given by (44). Using the same assumptions as above, we find

$$\tau_0 \approx \frac{\pi Y}{\sqrt{-\delta}}, \tag{54a}$$

$$\Delta U \approx \frac{64}{3}\frac{m\omega_0^2}{\gamma_1 + \gamma_3|a_m|^2} \times \left(\frac{y_j}{x_j}\right)^{-2}|a_m|^2\sqrt{1 + K^2}\,Y(-\delta)^{\frac{3}{2}}. \tag{54b}$$

Unlike in the previous approximations, one has to know at least the order of magnitude of the response amplitude in the vicinity of the jump point (in addition to effective noise temperature T and effective mass m) in order to approximate τ_{therm} appropriately. The same is also true for estimation attempt of the physical nonlinear constants

$$\alpha_3 = \frac{2\omega_0 \Delta\omega_m}{3|a_m|^2}, \tag{55a}$$

$$\gamma_3 = 2p\frac{\Delta\omega_m}{|a_m|^2}. \tag{55b}$$

For more accurate estimation, one of several existing kinds of fitting procedures can be utilized [41, 67]. However, the order of magnitude estimations often fully satisfy the practical requirements.

3.5 Experimental considerations

The above discussion of parameters' evaluation using experimental data, especially in frequency domain, emphasizes the importance of accurate frequency measurements. However, the slowing down of the oscillator's response near the bifurcation points poses strict limitations on the rates of excitation frequency or amplitude sweeps used in such measurements [94]. This is to say that special care must be taken by the experimentalist choosing a correct sweep rate for the measurement in order to obtain the smallest error possible. Fortunately, this error can easily be estimated based on our previous analysis.

Let r_{sweep} represent the frequency sweep rate in the frequency response measurement. For example, using network analyzer in part of our experiments, we define

$$r_{\mathrm{sweep}} = 2\pi\frac{\text{frequency span (Hz)}}{\text{sweep time (s)}}. \tag{56}$$

In order to estimate the inaccuracy, δ_{err}, in the measured value of the bifurcation point detuning, $\Delta\omega_j$, which results from nonzero frequency sweep rate, the following expression may be used:

$$\frac{|\delta_{\mathrm{err}}|}{r_{\mathrm{sweep}}} \approx \tau_{\mathrm{sd}}(\delta_{\mathrm{err}}),$$

whose solution is

$$\delta_{\mathrm{err}} \approx \left(\frac{\pi}{2}Y r_{\mathrm{sweep}}\right)^{\frac{2}{3}}. \tag{57}$$

Note that this error is a systematic one—the measured jump point will always be shifted in the direction of the frequency sweep. Obviously, the first step towards accurate measuring of $\Delta\omega_j$ is to ensure that the established value of the bifurcation point detuning does not change when the sweep rate is further reduced.

Another possible source of uncertainty in frequency measurements near the bifurcation point is the thermal escape process. The error introduced by this process tends to shift the measured jump point detuning in the direction opposite to the direction of the frequency sweep. Moreover, unlike the error arising from slowing down process, this inaccuracy cannot be totally eliminated by reducing the sweep rate. However, as will be shown in Sect. 4.2, in our case this error is negligible.

4 Results

4.1 Nonlinear damping

A typical measured response of the fundamental mode of a 200-µm long beam occurring at the resonance frequency of 123.2 kHz measured with $V_{\mathrm{DC}} = 20$ V and varying excitation amplitude is seen in Fig. 12. The linear regime is shown in the frequency response diagram and damping backbone curve depicted in Figs. 13 and 14, respectively, for a 125-µm long beam with fundamental mode resonant frequency 885.53 kHz and $V_{\mathrm{DC}} = 20$ V. We derive the value of $\gamma_1 = \omega_0/2Q$ from the linear response at low excitation amplitude and find $Q = 7200$ for 200-µm long beam and $Q = 13\,600$ for 125-µm long beam.

As shown in Sect. 3.4, the value of p can be estimated for different excitation amplitudes using (46) and (48). Typical results of applying these methods to experimental data from a micromechanical beam oscillator can be seen in Fig. 15. Using these procedures we find $p = 0.30 \pm 0.02$ for the 200-µm long beam and $p = 0.11 \pm 0.01$ for the 125-µm long beam. We also estimate p from the critical point detuning using (26c), and obtain $p = 0.29$ for the 200-µm long beam and $p = 0.11$ for the 125-µm long beam.

4.2 Parameter evaluation

In order to illustrate the procedures derived in Sect. 3.4, we evaluate the main parameters of slow envelope dynamics of the 125-µm long beam in a particular case

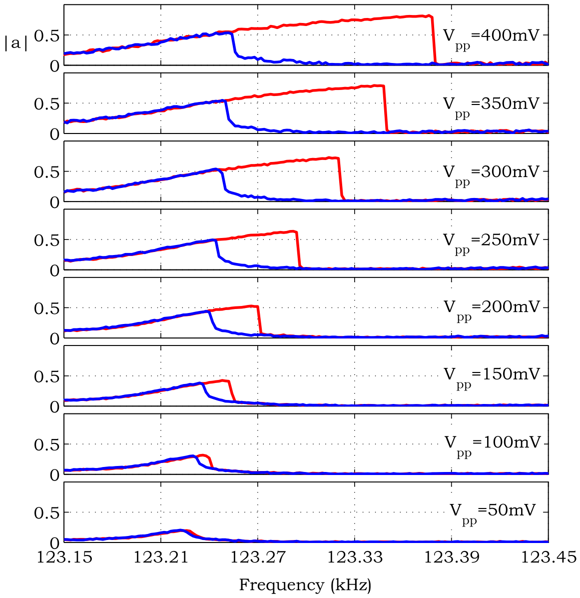

Fig. 12 Measured response amplitude vs. excitation frequency shown for both upward and downward frequency sweeps with $V_{\mathrm{DC}} = 20$ V and with varying peak-to-peak excitation amplitude v_{AC} of a 200-μm long beam with fundamental mode occurring at 123.2 kHz. The excitation amplitude is shown on the graphs. The oscillator exhibits bistable behavior at all excitation amplitudes except for the lowest one. *The vertical axis* is in arbitrary units

in which $V_{\mathrm{DC}} = 15$ V and the excitation voltage amplitude is 140 mV. The quality factor of the beam, as measured in the linear regime, is $Q = 13\,600$.

The results that can be derived from frequency measurements only, i.e., the results corresponding to (26c), (50) and (53), are summarized in Table 1.

For this measurement we employ a network analyzer with frequency span of 500 Hz, sweep time of 13.6 s, and bandwidth of 18 Hz. Therefore, the sweep rate defined in (56) is

$$r_{\mathrm{sweep}} = 2\pi \frac{500\ \mathrm{Hz}}{13.6\ \mathrm{s}} = 231\ \mathrm{rad\,s}^{-2}.$$

The inaccuracy in jump point detuning estimation due to slowing down process (see (57)) is

$$\frac{\delta_{\mathrm{err}}}{2\pi} \approx 2\ \mathrm{Hz}. \tag{58}$$

We now turn to estimate the order of magnitude of other parameters, including the nonlinear elastic constant α_3 and nonlinear damping constant γ_3. Based on the observations of the vibrating micromechanical beam by the means of SEM continuous scanning mode, we estimate the amplitude of mechanical vibration to be around 100 nm. The mass of a PdAu beam of the dimensions given in Sect. 2 is approximately 7×10^{-13} kg. These estimations allow us to assess the order of magnitude of several additional parameters shown in Table 2, which is based on (54) and (55).

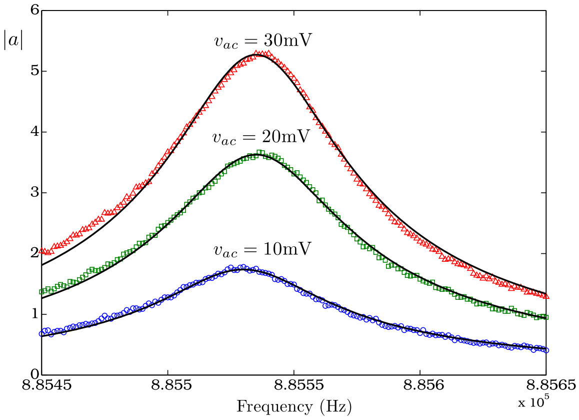

Fig. 13 (Color online) Measured frequency response in a linear regime of the 125-μm long beam with fundamental mode occurring at 885.53 kHz and $V_{\mathrm{DC}} = 15$ V. The linear regime is defined as a regime in which the frequency response function is symmetric around the resonance frequency. The measured responses with three different excitation amplitudes are shown. *Blue circles* correspond to $v = 10$ mV, *green rectangles* correspond to $v = 20$ mV, and *red triangles* correspond to $v = 30$ mV. *Solid black lines* show the fitted Lorentzian shapes. *Vertical scale* is in arbitrary units

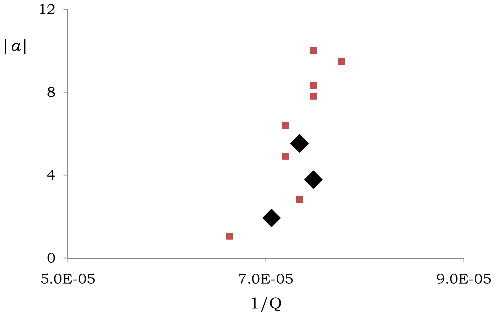

Fig. 14 Measured damping backbone curve of response vs. inverse quality factor $1/Q$ in a linear regime [4, 66]. *Large black diamonds* correspond to the frequency responses depicted in Fig. 13. The measured averaged quality factor is $Q = 13\,600 \pm 4\%$. Other experimental parameters are similar to those described in Fig. 13 caption. *Vertical scale* is in arbitrary units

We estimate below the thermal escape time for $\delta = -\delta_{\mathrm{err}}$ (see (58)). However, the value of the exponent, $\Delta U/k_B T \sim 6 \times 10^5$ at $T = 300$ K, makes the thermal escape time at this detuning value extremely large.

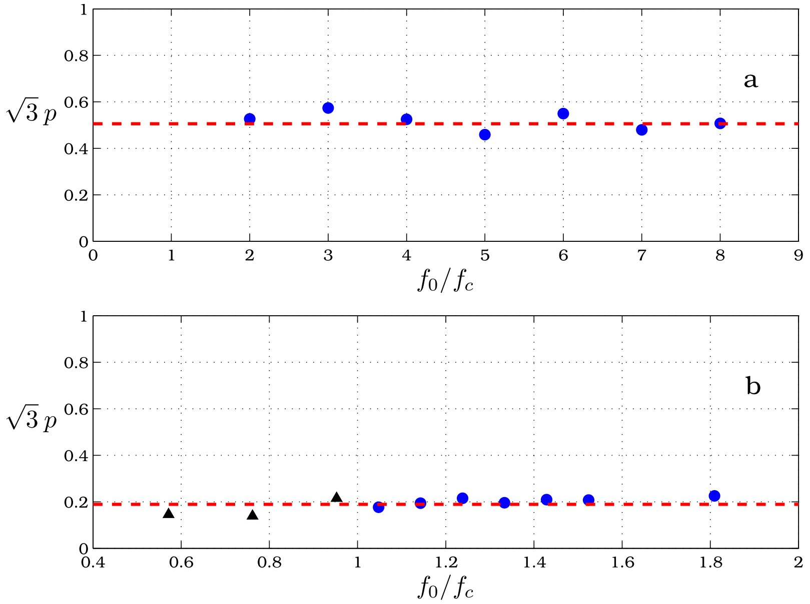

Fig. 15 (Color online) Experimental results for $p = \gamma_3\omega_0/3\alpha_3$ vs. excitation amplitude. The excitation amplitude on the horizontal axis is normalized by the respective critical excitation amplitude f_c. (**a**) 200-μm long beam with fundamental mode occurring at 123.20 kHz and $Q = 7200$. The values of p extracted from frequency domain jump point measurements (see (46)) are represented by *blue circles*. The average value is $p = 0.52/\sqrt{3} = 0.30 \pm 0.02$. *Red dashed line* represents the value of $p = 0.50/\sqrt{3} = 0.29$ evaluated using the critical point frequency detuning $\Delta\omega_c$ (see (26c)). The critical excitation voltage is 50 mV, and $V_{\mathrm{DC}} = 20$ V. (**b**) 120-μm long beam with fundamental mode occurring at 885.53 kHz and $Q = 13\,600$. The values of p extracted from time domain ring down measurements according to (48) and frequency domain jump point measurements (see (46)) are represented by *green squares* and *blue circles* respectively. The average value is $p = 0.19/\sqrt{3} = 0.11 \pm 0.01$. *Red dashed line* represents the value of $p = 0.19/\sqrt{3} = 0.11$ evaluated using the critical point frequency detuning $\Delta\omega_c$ that is given by (26c). The critical excitation voltage is 105 mV, and $V_{\mathrm{DC}} = 15$ V

Table 1 Parameters of the slow envelope dynamics of a 125-μm long beam. Applied DC voltage is 15 V and excitation voltage amplitude is 140 mV. The critical excitation voltage is 105 mV. Quality factor is $Q = 13\,600$. The uncertainty in $\Delta\omega_j$ is estimated using (58). The uncertainty in other parameters can be traced back to the uncertainty in the value of p, which is extracted from the experimental measurements (see Fig. 15b)

Parameter	Value	Units
$\omega_0/2\pi$	885534	Hz
γ_1	204	s^{-1}
$\Delta\omega_m/2\pi$	76	Hz
$\Delta\omega_j/2\pi$	81 ± 2	Hz
p	0.11 ± 0.01	
K	0.65 ± 0.03	
α	0.58 ± 0.02	rad
λ_f	-617 ± 25	s^{-1}
y_j/x_j	8.2 ± 0.2	
Y	0.158 ± 0.002	$\mathrm{s}^{-\frac{1}{2}}$

Therefore, in our experiments, the thermal escape process does not contribute significantly to the total inaccuracy in frequency measurements near the bifurcation point, at least for effective noise temperatures lower than 10^8 K, at which the assumption $\Delta \gg k_B T$ is no longer valid.

Finally, we compare the nonlinear dissipation term $\gamma_3|a|^2$ and the linear dissipation term γ_1 in the evolution equation (15). It follows from the above assumptions and the values in Table 2 that for our chosen example

$$\frac{\gamma_3|a_m|^2}{\gamma_1} \sim 0.1. \tag{59}$$

At this point, it is interesting to analyze the impact of the nonlinear damping on our experimental results by comparing them to the expected results that would have been measured if the nonlinear damping was absent, i.e., if $\gamma_3 = 0$ and, consequently, $p = 0$.

We use the fact that, as has been shown in Sect. 4.1, measuring the critical frequency detuning $\Delta\omega_c$ is a

Table 2 Order of magnitude estimation of parameters of a 125-μm long beam's slow envelope dynamics. The distance from the excitation frequency to the jump frequency is taken to be equal to δ_{err} (see (58)). Applied DC voltage is 15 V, the excitation voltage amplitude is 140 mV, and the estimated amplitude of vibration is 100 nm. The critical excitation voltage is 105 mV. Quality factor is $Q = 13\,600$

Parameter	Value at $\delta = -\delta_{\mathrm{err}} = -2\pi \times 2$ Hz	Units
α_3	2×10^{23}	$\mathrm{m^{-2}\,s^{-2}}$
γ_3	1×10^{16}	$\mathrm{m^{-2}\,s^{-1}}$
T	300	K
$\Delta U/k_B T$	6×10^5	
τ_0	0.13	s

reliable way to estimate the value of p. In our case, if the nonlinear damping was negligible, the critical frequency detuning would be equal to $\sqrt{3}\gamma_1/2\pi \approx 56$ Hz (see (26b)). However, the experimental value $\Delta\omega_c/2\pi = 74$ Hz is more than 30% larger, suggesting non-negligible nonlinear damping.

In order to further support the previous result, we plot the theoretical bistable frequency response of the micromechanical beam with and without nonlinear dissipation in Fig. 16. A significant difference between the two cases is evident.

4.3 Validity of the multiple scales approximation

In order to verify the correctness of our approximated solution achieved by multiple scales method, we compare the results of direct integration of the full motion equation (9) with the steady-state solution of the evolution equation (19). We use the results from Tables 1 and 2 for $\omega_0, \alpha_3, \gamma_1$, and γ_3. We also estimate the effective mass m to be 0.7×10^{-12} kg, the effective capacitance to be of order of $C_0 \approx 1.5 \times 10^{-15}$ F, the DC voltage $V_{\mathrm{DC}} = 15$ V, the AC voltage $v = 200$ mV, and take the distance d to be the actual distance between the electrode and the mechanical beam, i.e., $d = 5$ μm. The resulting excitation force amplitude is $f_0 = 600\ \mathrm{N\,kg^{-1}}$, the constant force is $F = 45\,000\ \mathrm{N\,kg^{-1}}$ (see (9)), and the constant resonance frequency shift is $\Delta\omega_0 = -2\pi \times 257$ Hz (see (14)).

In Fig. 16, the exact numerical integration of (9) is compared with the solution of the approximated frequency response equation (19). A very good correspondence between the two solutions is achieved, which validates the approximations applied in Sect. 3.2.

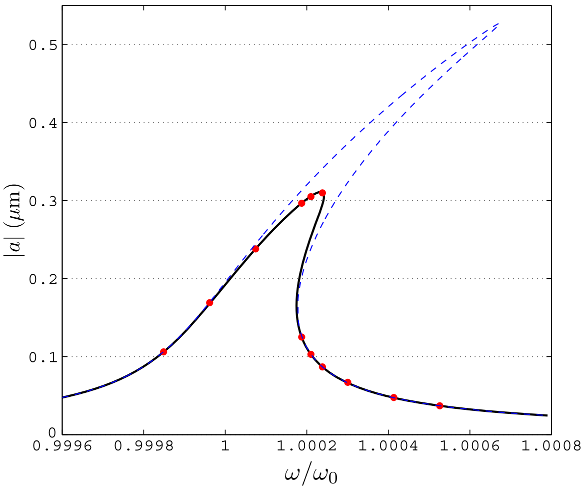

Fig. 16 (Color online) Comparison of numerically calculated steady-state response amplitude of the full equation of motion (9) (*red circles*) with the steady-state solution of the evolution equation (19) (*black solid line*). In addition, the steady-state solution under the same conditions except $\gamma_3 = 0$ (i.e., no nonlinear damping, $p = 0$) is plotted (*blue dashed line*) for comparison

In addition, the steady-state solution under the same conditions except $\gamma_3 = 0$ (i.e., no nonlinear damping, $p = 0$) is also plotted in Fig. 16. As discussed in Sect. 4.2, the existence of non-negligible nonlinear damping has a strong impact on the frequency response of the system, specifically on the locations of the jump points.

5 Discussion

5.1 Analysis of results

It follows from our experimental results that the nonlinear damping constant p can be estimated with a high degree of confidence by measuring the micromechanical oscillator bistable response in the frequency domain. The values of p that we find, $0.1 < p < 0.3$, obviously are not negligible. Referring to (26a) and (24), we see that the considered micromechanical oscillators exhibit a damping nonlinearity that has a measurable impact on both the amplitude and frequency offset of the critical point, as well as on jump points in the bistable region. On the other hand, these values are significantly smaller then the critical value $p =$

$1/\sqrt{3} \approx 0.577$, which would prevent the system from exhibiting bistable behavior.

Two methods of estimating the value of p from frequency domain measurements were used. The first is based on a single measurement of the critical point and provides a simple means for estimating the value of p by experimentally measuring the linear quality factor Q at low excitation amplitude and the critical frequency shift $\Delta\omega_c$ only (see (26c)). The second can be used for any excitation amplitude that drives the system into bistable regime, but requires a comparison of different response amplitudes (see (46)). Both these methods yield similar results; however, the second one, although being less accurate, allows the experimentalist to estimate when the limit of hard excitation [45] is approached and the first order multiple scales analysis used in this study becomes inadequate. In this limit of strong excitation, the extracted values of p start to diverge significantly from the results obtained at low excitation amplitudes. Our results, especially in Fig. 15, and the analysis of the validity of our approximations, which was carried out in Sect. 4.3, suggest that the analysis method employed by us is adequate for a wide range of excitation amplitudes.

The third method described above allows one to estimate the value of p from time domain measurements of the free ring down of the micromechanical beam oscillator based on (48). Although fitting results of time domain measurements to a theoretical curve introduce large inaccuracy, this method is invaluable in cases where the bistable regime cannot be achieved, e.g., due to prohibitively large amplitudes involved and the risk of pull-in.

By using the approximations developed in Sect. 3.4, we were able to estimate different parameters describing the slow envelope dynamics of our oscillators, summarized in Table 1. The most important and, as far as we know, novel result is the direct estimation of the slowing down time τ_{sd} that is given by (52), which governs the system's dynamics in the vicinity of bifurcation point. In turn, this result is used to quantitatively evaluate the error introduced to the frequency measurements by the slowing down process, δ_{err} that is given by (57), which in the example studied is 2 Hz. It can be seen that even slow sweeping rate (as compared to quasi-static rate in the linear case, which is of order of one resonant width per ring down time) can introduce a significant inaccuracy in the measured response of a micromechanical beam oscillator near bifurcation points. In our case, the inaccuracy in $\Delta\omega_j$ is about 3%, but the inaccuracy in $\Delta\omega_j - \Delta\omega_m$ is probably much larger.

The nonlinear damping constant p plays an important role in all the dynamical parameters. In the value of K that is given by (50a) in our example, p-dependent term constitutes about 30% of the value. The same is true for other parameters as well.

Also, we make order of magnitude estimations of thermal escape time τ_{thermal} (see (54)), α_3, and γ_3 (see (55)), which are summarized in Table 2. These approximations can be used in order to construct an accurate model of the effective one-dimensional movement of the system in the vicinity of a bifurcation point, especially if accurate enough estimations of the oscillator's amplitude and effective mass can be made.

In our case, only the order of magnitude of the parameters can be estimated. However, we were able to estimate the thermal escape time, and found the thermal escape process to be a non-negligible source of inaccuracy in the frequency measurements only at very high effective noise temperatures of order 10^8 K. This result can be compared to a result from our previous work [26]. In that work, a micromechanical beam oscillator similar to the ones used here was excited at a frequency between the bifurcation points. The intensity of voltage noise needed to cause transitions between these stable states was found to be $\approx$500 mV, with noise bandwidth of 10 MHz. The resulting voltage noise density is 158 $\mu\text{V}/\sqrt{\text{Hz}}$, which corresponds to an effective noise temperature $\sim 10^{13}$ K. In the case of thermal escape described here, the two stable states are highly asymmetrical. The effective noise temperature of 10^8 K, which invalidates the estimations of very slow thermal escape rate in Sect. 4.2, corresponds to voltage noise density of 0.5 $\mu\text{V}/\sqrt{\text{Hz}}$, giving the total voltage noise intensity of 1.6 mV.

Finally, we can also estimate the relative contribution of the nonlinear damping term $\gamma_3|a|^2$ in the evolution equation (15), and find it to be a non-negligible one tenth of the linear term γ_1 (see (59)) at the estimated amplitude of $|a| = 100$ nm.

5.2 Geometric nonlinearities as a source of nonlinear damping

The nature of nonlinear damping is not discussed in this work. However, nonlinear damping can be, in part, closely related to material behavior with a linear dissipation law that operates within a geometrically nonlinear regime. Here, we investigate one possible mechanism, originating from a Voigt–Kelvin type of dissipation model which describes internal viscoelastic damping in the form of a parallel spring and dashpot.

Before we proceed to build the model, one technical remark is in order. The notations in this section follow the standard ones used in continuum mechanics, and some parameters used above are redefined below. However, the end results are brought back to the form of (8).

Following Leamy and Gottlieb [95, 96], we consider a planar weakly nonlinear pre-tensioned, viscoelastic string augmented by linear Euler–Bernoulli bending, which incorporates a Voigt–Kelvin constitutive relationship where the stress is a linear function of the strain and strain rate [77, 97]:

$$\sigma = E\varepsilon + D\varepsilon_t,$$

where σ is the stress, ε is the strain, E is the material Young modulus, D is a viscoelastic damping parameter, and subscripts denote differentiation with respect to the corresponding variable. The equations of motion of the beam-string are

$$\rho A\tilde{u}_{tt} - \left[N\tilde{u}_{\tilde{s}} + EA\left(\tilde{u}_{\tilde{s}} + \frac{1}{2}\tilde{w}_{\tilde{s}}^2\right) + DA\left(\tilde{u}_{t\tilde{s}} + \tilde{w}_{\tilde{s}}\tilde{w}_{t\tilde{s}}\right)\right]_{\tilde{s}} = 0, \tag{60a}$$

$$\rho A\tilde{w}_{tt} - \left[N\tilde{w}_{\tilde{s}} + EA\tilde{w}_{\tilde{s}}\left(\tilde{u}_{\tilde{s}} + \frac{1}{2}\tilde{w}_{\tilde{s}}^2\right) + DA\tilde{w}_{\tilde{s}}(\tilde{u}_{t\tilde{s}} + \tilde{w}_{\tilde{s}}\tilde{w}_{t\tilde{s}}) - (EI\tilde{w}_{\tilde{s}\tilde{s}\tilde{s}} + DI\tilde{w}_{t\tilde{s}\tilde{s}\tilde{s}})\right]_{\tilde{s}} = Q_{\tilde{w}}, \tag{60b}$$

where N is the pre-tension, ρ is the material density, $\tilde{s}$ is the material coordinate along the beam, A and I are the elastic element cross-sectional area and moment of inertia, respectively. Also, $\tilde{u}(\tilde{s}, t)$ and $\tilde{w}(\tilde{s}, t)$ are the respective longitudinal and transverse components of an elastic field. The generalized transverse force component $Q_{\tilde{w}}$ is due to external electrodynamic actuation. Note that for a parallel plate approximation,

$$Q_{\tilde{w}} = B\frac{[V_{\mathrm{DC}} + v\cos(\omega t)]^2}{(d - \tilde{w})^2},$$

where V_{DC}, v, d and ω are as those defined in (8), and B is a proportionality coefficient dependent on the exact geometry of the mechanical oscillator.

We rescale the elastic field components $\tilde{u}$ and $\tilde{w}$, and the material coordinate $\tilde{s}$ by the beam length L, and time by the pre-tension $\sqrt{\rho AL^2/N}$ to yield a coupled set of dimensionless partial differential equations for the beam-string:

$$u_{\tau\tau} - \left[u_s + \beta\left(u_s + \frac{1}{2}w_s^2\right) + \delta(u_{\tau s} + w_s w_{\tau s})\right]_s = 0, \tag{61a}$$

$$w_{\tau\tau} - \left[w_s + \beta w_s\left(u_s + \frac{1}{2}w_s^2\right) + \delta w_s(u_{\tau s} + w_s w_{\tau s}) - (\alpha w_{sss} + \mu\delta w_{\tau sss})\right]_s = Q_w, \tag{61b}$$

where $u = \tilde{u}/L$, $w = \tilde{w}/L$, $s = \tilde{s}/L$ and

$$\tau = \omega_s t,$$

$$\omega_s^2 = \frac{N}{\rho AL^2}.$$

Other dimensionless parameters include the effects of weak bending $\alpha < 1$, a strong nonlinear pre-tension $\beta > 1$, a small slenderness ratio $\mu < 1$ (because $r/L \ll 1$, where $r = \sqrt{I/A}$ is the beam-string radius of gyration [97]), and finite viscoelastic damping δ:

$$\alpha = \frac{EI}{NL^2}, \qquad \beta = \frac{EA}{N}, \qquad \mu = \frac{I}{AL^2}, \qquad \delta = \frac{D}{L}\sqrt{\frac{\beta}{\rho E}}. \tag{62}$$

Note that $\sqrt{\beta}$ defines the ratio between the longitudinal and transverse wave speeds [45, 97]. The rescaled parallel plate approximation is thus

$$Q_w = \eta\frac{[1 + \epsilon\cos(\Omega t)]^2}{(\gamma - w)^2},$$

where

$$\eta = \frac{BV_{\mathrm{DC}}^2}{LN}, \qquad \Omega = \frac{\omega}{\omega_s}, \qquad \epsilon = \frac{v}{V_{\mathrm{DC}}},$$

$$\gamma = \frac{d}{L}.$$

We note that as the first longitudinal natural frequency is much higher than the first transverse natural frequency ($\beta \gg 1$), the longitudinal inertia and damping terms in (61a) can be neglected to yield a simple spatial relationship between the transverse and longitudinal derivatives. Incorporating fixed boundary conditions ($u(0,\tau) = u(1,\tau) = 0$) enables integration of the resulting relationship to yield

$$u_s = -\frac{1}{2}w_s^2 + c_1(\tau),$$

where

$$c_1 = \frac{1}{2}\int_0^1 w_s^2\,ds.$$

Thus, the resulting weakly nonlinear beam-string initial boundary value problem consists of an integro-differential equation for the transverse mode:

$$\begin{aligned} &w_{\tau\tau} - w_{ss}\big(1 + \beta c_1(\tau) + \delta c_{1\tau}(\tau)\big) \\ &\quad + \alpha w_{ssss} + \mu\delta w_{\tau ssss} = Q_w, \end{aligned} \tag{63}$$

where

$$c_{1\tau} = \int_0^1 w_s w_{\tau s}\,ds.$$

In order to facilitate comparison of the continuum model with the lumped mass model in (8), we consider a localized electrodynamic force $Q_w = Q_w(s = 1/2, \tau)$.

We reduce the integro-differential field equation in (63) and its fixed boundary conditions to a modal dynamical system via an assumed single mode Galerkin assumption, $w(s,\tau) = q_1(\tau)\phi_1(s)$, using a harmonic string mode $\phi_1 = \sqrt{2}\sin(\pi s)$:

$$\begin{aligned} &I_1 q_{\tau\tau} - I_2 q\left[1 + I_3\left(\frac{1}{2}\beta q^2 + \delta q q_\tau\right)\right] \\ &\quad + I_4(\alpha q + \mu\delta q_\tau) \\ &= I_5\eta\frac{[1 + \epsilon\cos(\Omega\tau)]^2}{(\gamma - I_5 q)^2}, \end{aligned} \tag{64}$$

where $q = q_1$ and the integral coefficients are:

$$I_1 = \int_0^1 \phi_1^2\,ds = 1,$$

$$I_2 = \int_0^1 \phi_1\phi_{1ss}\,ds = -\pi^2,$$

$$I_3 = \int_0^1 \phi_{1s}^2\,ds = \pi^2,$$

$$I_4 = \int_0^1 \phi_1\phi_{1ssss}\,ds = \pi^4,$$

$$I_5 = \phi_1\left(\frac{1}{2}\right) = \sqrt{2}.$$

It is convenient to rescale the maximal response $|w(1/2,\tau)| = q\bar{\phi}$, where $\bar{\phi} = \phi_1(1/2) = \sqrt{2}$, by the dimensionless gap $z = q\bar{\phi}/\gamma$, and to rescale time by the unperturbed ($\eta = 0$) natural frequency $t' = \tilde{\omega}_1\tau$, where $\tilde{\omega}_1 = \sqrt{\alpha I_4 - I_2} = \pi\sqrt{1 + \alpha\pi^2}$. The resulting dynamical system is

$$\ddot{z} + \left(\frac{1}{Q} + \hat{\delta}z^2\right)\dot{z} + \big(1 + \hat{\beta}z^2\big)z = \hat{\eta}\frac{[1 + \epsilon\cos(\hat{\Omega}t')]^2}{(1 - z)^2}, \tag{65}$$

where

$$\hat{\beta} = \frac{|I_2|I_3\beta\gamma^2}{2\bar{\phi}^2\tilde{\omega}_1^2}, \qquad \frac{1}{Q} = \frac{I_4\mu\delta}{\tilde{\omega}_1}, \qquad \hat{\delta} = \frac{\delta|I_2|I_3\gamma^2}{\bar{\phi}^2\tilde{\omega}_1},$$

$$\hat{\eta} = \frac{I_5\eta\bar{\phi}}{\gamma^3\tilde{\omega}_1^2}, \qquad \hat{\Omega} = \frac{\Omega}{\tilde{\omega}_1}.$$

Note that the ratio between nonlinear and linear damping in (65) consists of only the beam-string geometric properties [98]. For example, a typical ratio is $\hat{\delta}Q = 6d^2/h^2 \approx 65$ for a beam-string with a prismatic cross section, where $h = 1.5$ μm is the dimension of the beam-string in the transverse direction w, and $d = 5$ μm is the resonator gap.

The last equation (65) can be compared, after rescaling, to the dimensional equation (8), which we rewrite here for convenience after some rearrangement and simplification (e.g. $\gamma_{32} = 0$):

$$\begin{aligned} &\ddot{x} + \big(2\gamma_{11} + \gamma_{31}x^2\big)\dot{x} + \big(\omega_0^2 + \alpha_3 x^2\big)x \\ &\quad = \frac{C_0 V_{\mathrm{DC}}^2}{2md}\frac{\big[1 + \frac{v}{V_{\mathrm{DC}}}\cos\omega t\big]^2}{\big(1 - \frac{x}{d}\big)^2}. \end{aligned} \tag{66}$$

The comparison of (65) with (66) results in:

$$\alpha_3 = \frac{\hat{\beta}\omega_0^2}{d^2} = \frac{\pi^2 EA\omega_0^2}{4NL^2} = \frac{\pi^2\alpha A\omega_0^2}{4I}, \tag{67a}$$

$$\gamma_{11} = \frac{\omega_0}{2Q}, \tag{67b}$$

$$\gamma_{31} = \frac{\hat{\delta}\omega_0}{d^2} = \frac{A\gamma_{11}}{I}, \tag{67c}$$

$$F = \frac{C_0 V_{\mathrm{DC}}^2}{2md} = \hat{\eta}\, d\omega_0^2. \tag{67d}$$

The last results can be used to estimate the lower bound of nonlinear damping due to nonlinear pretension of a viscoelastic string. Using (17), (62), (67), and

$$I = \frac{Ah^2}{12}$$

for prismatic cross section, one has

$$p_{\min} = \frac{2}{3}\frac{\tilde{\omega}_1 \delta}{\beta} \approx \frac{8}{\pi^2}\frac{1}{Q}\left(\frac{L}{h}\right)^2 \frac{N}{EA} = \frac{2}{3\pi^2 Q\alpha}, \tag{68}$$

where h denotes the dimension of the beam-string in the transverse direction w.

It is possible to estimate the order of magnitude of $p_{\min}$ in (68) for metals using the fact that the Young modulus of bulk metals $E \sim O(10^{10})$–$O(10^{11})$ Pa. Also, the largest value of N/A that is still compatible with elastic behavior can be approximated by half the ultimate tensile strength, which is about 50–100×10^6 Pa for most metals. For our beam-strings discussed above, $L = 100$–200 µm, $h \approx 1$ µm. Using these values results in $p \sim O(10^{-4})$–$O(10^{-3})$. For longer and wider beams ($L = 500$ µm, $h = 1.5$ µm) fabricated and measured using the same methods [98], the lower bound on nonlinear damping coefficient given by (68) is $p_{\min} \sim 0.0022$–0.045, while the range of values extracted from the experiment is $0.015 < p < 0.151$ [98]. Although the elastic properties of a specific metal or alloy used in micro-machined devices might differ significantly from the bulk values, they are still likely to fall inside the ranges defined above. Therefore, a linear viscoelastic process with a pure Voigt–Kelvin dissipation model can serve as a possible lower bound but cannot account for the main part of nonlinear dissipation rate found in our experiments.

Unfortunately, theory describing the processes underlying nonlinear damping in micromechanical beam is virtually non-existent at this moment, and no clear tendencies in the value of p were observed during the experiments. Therefore, the exact behavior of nonlinear damping term during beam scaling and its dependence on the linear Q of the structure remains elusive. Further experiments with wider range of micromechanical beams are needed to establish this behavior and to pinpoint the most significant mechanisms of dissipation.

6 Summary

In this study, the nonlinear dynamical behavior of an electrically excited micromechanical doubly clamped beam oscillator was investigated in vacuum. The micromechanical beam was modeled as a Duffing-like single degree of freedom oscillator, nonlinearly coupled to a thermal bath. Using the method of multiple scales, we were able to construct a detailed model of slow envelope behavior of the system, including effective noise terms.

It follows from the model that nonlinear damping plays an important role in the dynamics of the micromechanical beam oscillator. Several methods for experimental evaluation of the contribution of the nonlinear damping were proposed, applicable at different experimental situations. These methods were compared experimentally and shown to provide similar results. The experimental values of the nonlinear damping constant are non-negligible for all the beams measured.

Also, the slow envelope model was used to describe the behavior of the system close to bifurcation points in the presence of nonlinear damping. In the vicinity of these points, the dynamics of the system is significantly slowed down, and the phase plane motion becomes essentially one-dimensional. We have defined several parameters that govern the dynamics of the micromechanical beam oscillator in these conditions, and have provided simple approximations that can be used to estimate these parameters from experimental data.

The approximations developed in this study can be utilized by the experimentalist in order to estimate the inaccuracy of frequency response measurements of Duffing-like oscillators in the vicinity of bifurcation points. Applying these results to our samples, we have found that thermal escape process near the bifurcation point causes measurement inaccuracy that is negligible. In contrast, the slowing down phenomenon, which is a characteristic of saddle-node bifurcation, can contribute a significant error to the measured frequency response. This error is non-negligible even at relatively slow frequency sweeping rates. Similar methods can be utilized for other parameter sweeping measurements, such as excitation amplitude sweeping.

As part of an effort to explain the origins of the nonlinear damping, we have formulated and analyzed a model of a planar, weakly nonlinear pretensioned, viscoelastic string augmented by linear Euler–Bernoulli bending, which incorporates a Voigt–Kelvin constitutive relationship. This model exemplifies one of the possible causes of non-negligible nonlinear damping observed in the experiment. Based on this model, we have determined a simple relation connecting the maximal expected value of the nonlinear damping parameter, the bulk Young modulus of the material, and its yielding stress. However, while this model can serve as a lower bound, it cannot account for the full magnitude of the nonlinear damping measured in the experiment. Additional experimental and theoretical work is required to enhance our understanding of the phenomenon of nonlinear damping in microelectromechanical systems.

In this work we have demonstrated conclusively that nonlinear damping in micromechanical doubly-clamped beam oscillator may play an important role. The methods presented in this paper may allow a systematic study of nonlinear damping in micro- and nano-mechanical oscillators, which may help revealing the underlying physical mechanisms.

Acknowledgements We would like to thank R. Lifshitz for many fruitful discussions. This work was partially supported by Intel Corporation, the Israeli Ministry of Science, the Israel Science foundation, the German Israel foundation, and the Russell Berry foundation.

References

1. Turner, K.L., Miller, S.A., Hartwell, P.G., MacDonald, N.C., Strogatz, S.H., Adams, S.G.: Five parametric resonances in a microelectromechanical system. Nature **396**, 149–152 (1998)
2. Roukes, M.: Nanoelectromechanical systems face the future. Phys. World **14**, 25–25 (2001)
3. Roukes, M.: Nanomechanical systems. Technical digest of the 2000 solid state sensor and actuator workshop (2000)
4. Husain, A., Hone, J., Postma, H.W.C., Huang, X.M.H., Drake, T., Barbic, M., Scherer, A., Roukes, M.L.: Nanowire-based very-high-frequency electromechanical resonator. Appl. Phys. Lett. **83**, 1240–1242 (2003)
5. Sidles, J.A., Garbini, J.L., Bruland, K.J., Rugar, D., Zuger, O., Hoen, S., Yannoni, C.S.: Magnetic resonance force microscopy. Rev. Mod. Phys. **67**(1), 249–265 (1995)
6. Rugar, D., Budakian, R., Mamin, H.J., Chui, B.W.: Single spin detection by magnetic resonance force microscopy. Nature **430**, 329–332 (2004)
7. Ekinci, K.L., Yang, Y.T., Roukes, M.L.: Ultimate limits to inertial mass sensing based upon nanoelectromechanical systems. J. Appl. Phys. **95**(5), 2682–2689 (2004)
8. Ekinci, K.L., Huang, X.M.H., Roukes, M.L.: Ultrasensitive nanoelectromechanical mass detection. Appl. Phys. Lett. **84**(22), 4469–4471 (2004)
9. Ilic, B., Craighead, H.G., Krylov, S., Senaratne, W., Ober, C.: Attogram detection using nanoelectromechanical oscillators. J. Appl. Phys. **95**, 3694 (2004)
10. Nayfeh, A.H., Ouakad, H.M., Najar, F., Choura, S., Abdel-Rahman, E.M.: Nonlinear dynamics of a resonant gas sensor. Nonlinear Dyn. **59**(4), 607–618 (2010)
11. Blencowe, M.: Quantum electromechanical systems. Phys. Rep. **395**, 159–222 (2004)
12. Knobel, R.G., Cleland, A.N.: Nanometre-scale displacement sensing using a single electron transistor. Nature **424**, 291–293 (2003)
13. LaHaye, M.D., Buu, O., Camarota, B., Schwab, K.C.: Approaching the quantum limit of a nanomechanical resonator. Science **304**, 74–77 (2004)
14. Schwab, K., Henriksen, E.A., Worlock, J.M., Roukes, M.L.: Measurement of the quantum of thermal conductance. Nature **404**, 974–977 (2000)
15. Buks, E., Roukes, M.L.: Stiction, adhesion energy, and the Casimir effect in micromechanical systems. Phys. Rev. B **63**, 33402 (2001)
16. Buks, E., Roukes, M.L.: Metastability and the Casimir effect in micromechanical systems. Europhys. Lett. **54**(2), 220–226 (2001)
17. Schwab, K.C., Roukes, M.L.: Putting mechanics into quantum mechanics. Phys. Today **58**, 36–42 (2005)
18. Aspelmeyer, M., Schwab, K.: Focus on mechanical systems at the quantum limit. New J. Phys. **10**(9), 095001 (2008)
19. Kozinsky, I., Postma, H.W.C., Kogan, O., Husain, A., Roukes, M.L.: Basins of attraction of a nonlinear nanomechanical resonator. Phys. Rev. Lett. **99**, 207201 (2007)
20. Cross, M.C., Zumdieck, A., Lifshitz, R., Rogers, J.L.: Synchronization by nonlinear frequency pulling. Phys. Rev. Lett. **93**, 224101 (2004)
21. Erbe, A., Krömmer, H., Kraus, A., Blick, R.H., Corso, G., Richter, K.: Mechanical mixing in nonlinear nanomechanical resonators. Appl. Phys. Lett. **77**, 3102–3104 (2000)
22. Rhoads, J.F., Shaw, S.W., Turner, K.L., Baskaran, R.: Tunable microelectromechanical filters that exploit parametric resonance. J. Vib. Acoust. **127**, 423–431 (2005)
23. Reichenbach, R.B., Zalalutdinov, M., Aubin, K.L., Rand, R., Houston, B.H., Parpia, J.M., Craighead, H.G.: Third-order intermodulation in a micromechanical thermal mixer. J. Micro/Nanolithogr. MEMS MOEMS **14**, 1244–1252 (2005)
24. Almog, R., Zaitsev, S., Shtempluck, O., Buks, E.: High intermodulation gain in a micromechanical Duffing resonator. Appl. Phys. Lett. **88**, 213509 (2006)
25. Almog, R., Zaitsev, S., Shtempluck, O., Buks, E.: Noise squeezing in a nanomechanical Duffing resonator. Phys. Rev. Lett. **98**, 78103 (2007)
26. Almog, R., Zaitsev, S., Shtempluck, O., Buks, E.: Signal amplification in a nanomechanical duffing resonator via stochastic resonance. Appl. Phys. Lett. **90**, 13508 (2007)
27. Zhang, W., Baskaran, R., Turner, K.L.: Nonlinear behavior of a parametric resonance-based mass sensor. In: Proc. IMECE2002, p. 33261 Nov (2002)

28. Buks, E., Yurke, B.: Mass detection with nonlinear nanomechanical resonator. Phys. Rev. E **74**, 46619 (2006)
29. Cleland, A.N., Roukes, M.L.: Noise processes in nanomechanical resonators. J. Appl. Phys. **92**(5), 2758–2769 (2002)
30. Yasumura, K.Y., Stowe, T.D., Chow, E.M., Pfafman, T., Kenny, T.W., Stipe, B.C., Rugar, D.: Quality factors in micron- and submicron-thick cantilevers. J. Micromech. Syst. **9**(1), 117–125 (2000)
31. Ono, T., Wang, D.F., Esashi, M.: Time dependence of energy dissipation in resonating silicon cantilevers in ultrahigh vacuum. Appl. Phys. Lett. **83**(10), 1950–1952 (2003)
32. Liu, X., Thompson, E., White, B. Jr, Pohl, R.: Low-temperature internal friction in metal films and in plastically deformed bulk aluminum. Phys. Rev. B **59**(18), 11767–11776 (1999)
33. Harrington, D.A., Mohanty, P., Roukes, M.L.: Energy dissipation in suspended micromechanical resonators at low temperatures. Physica B **284–288**, 2145–2146 (2000)
34. Lifshitz, R., Roukes, M.L.: Thermoelastic damping in micro- and nanomechanical systems. Phys. Rev. B **61**(8), 5600–5609 (2000)
35. Houston, B.H., Photiadis, D.M., Marcus, M.H., Bucaro, J.A., Liu, X., Vignola, J.F.: Thermoelastic loss in microscale oscillators. Appl. Phys. Lett. **80**(7), 1300–1302 (2002)
36. Lifshitz, R.: Phonon-mediated dissipation in micro- and nano-mechanical systems. Physica B **316–317**, 397–399 (2002)
37. Wilson-Rae, I.: Intrinsic dissipation in nanomechanical resonators due to phonon tunneling. Phys. Rev. B **77**, 245418 (2008)
38. Remus, L.G., Blencowe, M.P., Tanaka, Y.: Damping and decoherence of a nanomechanical resonator due to a few two level systems. arXiv:0907.0431 [cond-mat] (2009)
39. Popovic, P., Nayfeh, A.H., Oh, K., Nayfeh, S.A.: An experimental investigation of energy transfer from a highfrequency mode to a low-frequency mode in a flexible structure. J. Vib. Control **1**(1), 115–128 (1995)
40. Hajj, M.R., Fung, J., Nayfeh, A.H., Fahey, S.O.: Damping identification using perturbation techniques and higher-order spectra. Nonlinear Dyn. **23**(2), 189–203 (2000)
41. Jaksic, N., Boltezar, M.: An approach to parameter identification for a single-degree-of-freedom dynamical system based on short free acceleration response. J. Sound Vib. **250**, 465–483 (2002)
42. Zhang, W., Baskaran, R., Turner, K.L.: Effect of cubic nonlinearity on auto-parametrically amplified resonant MEMS mass sensor. Sens. Actuators A, Phys. **102**, 139–150 (2002)
43. Zhang, W., Baskaran, R., Turner, K.: Tuning the dynamic behavior of parametric resonance in a micromechanical oscillator. Appl. Phys. Lett. **82**, 130–132 (2003)
44. Krylov, S., Ilic, B.R., Schreiber, D., Seretensky, S., Craighead, H.: The pull-in behavior of electrostatically actuated bistable microstructures. J. Micromech. Microeng. **18**(5), 055026 (2008)
45. Nayfeh, A.H., Mook, D.T.: Nonlinear Oscillations. Wiley, New York (1995). Wiley Classics Library
46. Dykman, M., Krivoglaz, M.: Theory of nonlinear oscillator interacting with a medium. In: Khalatnikov, I.M. (ed.) Soviet Scientific Reviews, Section A, Physics Reviews, vol. 5, pp. 265–441. Harwood Academic, Reading (1984)
47. Landau, L.D., Lifshitz, E.M.: Mechanics, 3rd edn. Pergamon, New York (1976)
48. Nayfeh, A.H.: Introduction to Perturbation Techniques. Wiley, New York (1981)
49. Arnold, V.I.: Geometrical methods in the theory of ordinary differential equations, Grundlehren der mathematischen Wissenschaften, vol. 250, 2nd edn. Springer, New York (1988)
50. Strogatz, S.H.: Nonlinear Dynamics and Chaos: With Applications to Physics, Biology, Chemistry, and Engineering. Perseus Books, Readings (1994)
51. Chan, H.B., Dykman, M., Stambaugh, C.: Paths of fluctuation induced switching. Phys. Rev. Lett. **100**, 130602 (2008)
52. Dykman, M.I., Golding, B., Ryvkine, D.: Critical exponent crossovers in escape near a bifurcation point. Phys. Rev. Lett. **92**(8), 080602 (2004)
53. Yurke, B., Buks, E.: Performance of cavity-parametric amplifiers, employing Kerr nonlinearites, in the presence of two-photon loss. J. Lightwave Technol. **24**(12), 5054–5066 (2006)
54. Buks, E., Yurke, B.: Dephasing due to intermode coupling in superconducting stripline resonators. Phys. Rev. A **73**, 23815 (2006)
55. Ravindra, B., Mallik, A.K.: Role of nonlinear dissipation in soft Duffing oscillators. Phys. Rev. E **49**(6), 4950–4953 (1994)
56. Ravindra, B., Mallik, A.K.: Stability analysis of a nonlinearly damped Duffing oscillator. J. Sound Vib. **171**(5), 708–716 (1994)
57. Trueba, J.L., Rams, J., Sanjuan, M.A.F.: Analytical estimates of the effect of nonlinear damping in some nonlinear oscillators. Int. J. Bifurc. Chaos **10**(9), 2257–2267 (2000)
58. Baltanas, J.P., Trueba, J.L., Sanjuan, M.A.F.: Energy dissipation in a nonlinearly damped Duffing oscillator. Physica D **159**, 22–34 (2001)
59. Sanjuan, M.A.F.: The effect of nonlinear damping on the universal escape oscillator. Int. J. Bifurc. Chaos **9**(4), 735–744 (1999)
60. Krylov, S., Maimon, R.: Pull-in dynamics of an elastic beam actuated by continuously distributed electrostatic force. J. Vib. Acoust. **126**, 332–343 (2004)
61. Jing, X.J., Lang, Z.Q.: Frequency domain analysis of a dimensionless cubic nonlinear damping system subject to harmonic input. Nonlinear Dyn. **58**(3), 469–485 (2009)
62. Lifshitz, R., Cross, M.: Nonlinear dynamics of nanomechanical and micromechanical resonators. In: Schuster, H.G. (ed.) Reviews of nonlinear dynamics and complexity, vol. 1, pp. 1–48. Wiley-VCH, New York (2008)
63. Gutschmidt, S., Gottlieb, O.: Internal resonances and bifurcations of a microbeam array below the first pull-in instability. Int. J. Bifurc. Chaos **20**(3), 605–618 (2010)
64. Lifshitz, R., Cross, M.C.: Response of parametrically driven nonlinear coupled oscillators with application to micromechanical and nanomechanical resonator arrays. Phys. Rev. B **67**, 134302 (2003)
65. Bikdash, M., Balachandran, B., Nayfeh, A.: Melnikov analysis for a ship with a general roll-damping model.Nonlinear Dyn. **6**, 101–124 (1994)
66. Gottlieb, O., Feldman, M.: Application of a Hilbert transform-based algorithm for parameter estimation of a

nonlinear ocean system roll model. J. Offshore Mech. Arct. Eng. **119**, 239–243 (1997)
67. Dick, A.J., Balachandran, B., DeVoe, D.L., Mote, C.D. Jr.: Parametric identification of piezoelectric microscale resonators. J. Micromech. Microeng. **16**, 1593–1601 (2006)
68. Zhu, W.Q., Wu, Y.J.: First-passage time of duffing oscillator under combined harmonic and white-noise excitations. Nonlinear Dyn. **32**(3), 291–305 (2003)
69. Aldridge, J., Cleland, A.: Noise-enabled precision measurements of a Duffing nanomechanical resonator. Phys. Rev. Lett. **94**, 156403 (2005)
70. Younis, M.I., Nayfeh, A.H.: A study of the nonlinear response of a resonant microbeam to an electric actuation. Nonlinear Dyn. **31**(1), 91–117 (2003)
71. Buks, E., Roukes, M.L.: Electrically tunable collective response in a coupled micromechanical array. J. Micromech. Syst. **11**(6), 802–807 (2002)
72. Ullersma, P.: An exactly solvable model for Brownian motion: I. derivation of the Langevin equation. Physica **32**, 27–55 (1966)
73. Ullersma, P.: An exactly solvable model for Brownian motion: II. derivation of the Fokker-Planck equation and the master equation. Physica **32**, 56–73 (1966)
74. Caldeira, A.O., Leggett, A.J.: Path integral approach to quantum Brownian motion. Physica A **121**, 587–616 (1983)
75. Hänggi, P.: Generalized Langevin equations: A useful tool for the perplexed modeller of nonequilibrium fluctuations? In: Stochastic Dynamics. Lecture Notes in Physics, vol. 484, pp. 15–22. Springer, Berlin (1997)
76. Mohanty, P., Harrington, D.A., Ekinci, K.L., Yang, Y.T., Murphy, M.J., Roukes, M.L.: Intrinsic dissipation in high-frequency micromechanical resonators. Phys. Rev. B **66**, 85416 (2002)
77. Zener, C.: Elasticity and Anelasticity of Metals. The University of Chicago Press, Chicago (1948)
78. Stievater, T.H., Rabinovich, W.S., Papanicolaou, N.A., Bass, R., Boos, J.B.: Measured limits of detection based on thermal-mechanical frequency noise in micromechanical sensors. Appl. Phys. Lett. **90**, 051114 (2007)
79. Ke, T.: Stress relaxation across grain boundaries in metals. Phys. Rev. **72**(1), 41–46 (1947)
80. Ono, T., Esashi, M.: Effect of ion attachment on mechanical dissipation of a resonator. Appl. Phys. Lett. **87**(44105) (2005)
81. Zolfagharkhani, G., Gaidarzhy, A., Shim, S., Badzey, R.L., Mohanty, P.: Quantum friction in nanomechanical oscillators at millikelvin temperatures. Phys. Rev. B **72**, 224101 (2005)
82. Geller, M.R., Varley, J.B.: Friction in nanoelectromechanical systems: Clamping loss in the GHz regime. arXiv:cond-mat/0512710 (2005)
83. Cross, M., Lifshitz, R.: Elastic wave transmission at an abrupt junction in a thin plate with application to heat transport and vibrations in mesoscopic systems. Phys. Rev. B **64**, 85324 (2001)
84. Hänggi, P., Ingold, G.L.: Fundamental aspects of quantum Brownian motion. Chaos **15**(2), 026105 (2005)
85. Landau, L.D., Lifshitz, E.M.: Statistical Physics, Part 1, 3rd edn. Pergamon, New York (1980)
86. Kubo, R.: The fluctuation-dissipation theorem. Rep. Prog. Phys. **29**, 255–284 (1966)
87. Chandrasekhar, S.: Stochastic problems in physics and astronomy. Rev. Mod. Phys. **15**(1), 1–89 (1943)
88. Klimontovich, Y.L.: Statistical Theory of Open Systems: Volume 1: A Unified Approach to Kinetic Description of Processes in Active Systems. Kluwer Academic, Norwell (1995)
89. Habib, S., Kandrup, H.: Nonlinear noise in cosmology. Phys. Rev. D **46**, 5303–5314 (1992)
90. Yurke, B., Greywall, D.S., Pargellis, A.N., Busch, P.A.: Theory of amplifier-noise evasion in an oscillator employing nonlinear resonator. Phys. Rev. A **51**(5), 4211–4229 (1995)
91. Rugar, D., Grüetter, P.: Mechanical parametric amplification and thermomechanical noise squeezing. Phys. Rev. Lett. **67**, 699–702 (1991)
92. Kramers, H.A.: Brownian motion in a field of force and the diffusion model of chemical reactions. Physica **7**, 284–304 (1940)
93. Hänggi, P., Talkner, P., Borkovec, M.: Reaction-rate theory: fifty years after Kramers. Rev. Mod. Phys. **62**, 251–342 (1990)
94. Kogan, O.: Controlling transitions in a Duffing oscillator by sweeping parameters in time. Phys. Rev. E **76**, 037203 (2007)
95. Leamy, M.J., Gottlieb, O.: Internal resonances in whirling strings involving longitudinal dynamics and material nonlinearities. J. Sound Vib. **236**, 683–703 (2000)
96. Leamy, M.J., Gottlieb, O.: Nonlinear dynamics of a taut string with material nonlinearities. J. Vib. Acoust. **123**, 53–60 (2001)
97. Meirovitch, L.: Principles and Techniques of Vibrations. Prentice-Hall, New York (1997)
98. Mintz, T.: Nonlinear dynamics and stability of a microbeam array subject to parametric excitation. Master's thesis, Technion – Israel Institute of Technology (2009)